JGR Earth Surface

RESEARCH ARTICLE
10.1029/2025JF008720

Key Points:

- Enhanced digital elevation model differencing using NASADEM captures erosion patterns in the Laonong Basin after vegetation and vertical bias correction
- Substantial sediment buffering and valley-fill aggradation delay sediment export despite high local erosion in sub-catchments
- Decadal erosion rates match millennial averages despite extreme events, consistent with the influence of landscape buffering mechanisms

Supporting Information:

Supporting Information may be found in the online version of this article.

Correspondence to:

Y.-C. Chan,
yuchang@earth.sinica.edu.tw

Citation:

Kumar, G., Chan, Y.-C., Sun, C.-W., & Chen, C.-T. (2026). Decadal Erosion rates and sediment buffering identified through enhanced DEM differencing using underutilized global satellite DEMs. *Journal of Geophysical Research: Earth Surface*, *131*, e2025JF008720. https://doi.org/10.1029/2025JF008720

Received 12 SEP 2025
Accepted 21 APR 2026

Author Contributions:

Conceptualization: Gopal Kumar, Yu-Chang Chan
Data curation: Gopal Kumar, Yu-Chang Chan, Cheng-Wei Sun
Formal analysis: Gopal Kumar, Yu-Chang Chan
Funding acquisition: Yu-Chang Chan
Investigation: Gopal Kumar, Yu-Chang Chan, Chih-Tung Chen
Methodology: Gopal Kumar, Yu-Chang Chan, Cheng-Wei Sun
Project administration: Yu-Chang Chan
Resources: Gopal Kumar, Yu-Chang Chan, Chih-Tung Chen

Decadal Erosion Rates and Sediment Buffering Identified Through Enhanced DEM Differencing Using Underutilized Global Satellite DEMs

Gopal Kumar[1,2,3], Yu-Chang Chan[1,2], Cheng-Wei Sun[2,4], and Chih-Tung Chen[1,3]

[1]Taiwan International Graduate Program (TIGP), Academia Sinica, Taipei, Taiwan, [2]Institute of Earth Sciences, Academia Sinica, Taipei, Taiwan, [3]Department of Earth Sciences, National Central University, Taoyuan, Taiwan, [4]Department of Geosciences, National Taiwan University, Taipei, Taiwan

Abstract Quantifying decadal-scale erosion rates in tectonically active regions is essential for assessing landscape hazards and constraining sediment budgets. A key question in Earth surface processes is how contemporary erosion measurements influenced by recent climatic extremes relate to long-term geological rates. This study investigates this relationship by evaluating two decades of topographic change (2000–2020) in Taiwan's Laonong River Basin (1,373 km^2), a mountainous landscape characterized by active landslides, steep relief, and intense rainfall, including Typhoon Morakot in 2009, the highest-rainfall typhoon on record in Taiwan. Several satellite-derived digital elevation models (DEMs) were benchmarked against high-resolution LiDAR to identify the most suitable data set for long-term change detection. The reprocessed SRTM NASADEM was identified as the optimal DEM due to minimal artifacts and limited void filling, with further improvement achieved through canopy removal and frequency-domain bias correction. DEM differencing across sub-catchments revealed that erosion rates averaged ∼15.3 mm/yr, reaching ∼551 mm/yr in landslide-affected tributaries. However, approximately 87.6% of the eroded material was stored within the basin, predominantly in valley-fill deposits, reducing effective net lowering across the basin to 5.06 ± 1.60 mm/yr. This rate is consistent with long-term (10^3–10^6 yr) cosmogenic and thermochronological estimates (∼3–6 mm/yr), indicating that sediment buffering spatially averages extreme localized erosion over decadal timescales. These findings highlight the role of internal sediment storage in shaping basin-scale erosion patterns and emphasize the importance of high-resolution erosion assessments for capturing geomorphic heterogeneity. The results also demonstrate the potential of underutilized global DEMs, once corrected, to resolve meaningful geomorphic signals in mountainous terrain.

Plain Language Summary Recent climate change has increased extreme rainfall events, raising interest in how quickly mountain landscapes are eroding. A key uncertainty is whether erosion rates measured over decades during such events systematically exceed longer-term rates derived over thousands to millions of years. We explored this question in Taiwan's Laonong Basin, a mountainous region frequently impacted by landslides and heavy rainfall. By analyzing satellite-based elevation models, we identified a recently reprocessed elevation data set collected in February 2000 as the most reliable option for accurately measuring how fast the landscape is eroding. The estimated decadal erosion rate for the Laonong Basin is about 5 mm per year, consistent with longer-term geological estimates. This agreement shows that, even during decades with major storms, sediment tends to be stored in valleys and debris fans before being exported, keeping short-term and long-term erosion rates in balance. Sub-catchments within the basin showed much higher erosion rates, pointing to local landslide hazards that are averaged out at the basin scale. These findings highlight the role of sediment storage in shaping erosion patterns and show that, once corrected for biases, freely available satellite elevation data sets provide a valuable tool for reconstructing decadal-scale geomorphic change in data-sparse mountainous regions.

1. Introduction

Landscape evolution occurs through the fundamental relationship between erosional sediment flux and surface lowering (Molnar & England, 1990; Willett, 1999). Estimating erosion rates across different temporal scales therefore provides essential insights into the processes and controls governing land surface change. Multiple approaches exist for measuring erosional processes across different temporal domains, including suspended

Software: Gopal Kumar, Yu-Chang Chan, Cheng-Wei Sun
Supervision: Yu-Chang Chan
Validation: Gopal Kumar, Yu-Chang Chan, Cheng-Wei Sun
Visualization: Gopal Kumar, Yu-Chang Chan
Writing – original draft: Gopal Kumar, Yu-Chang Chan
Writing – review & editing: Gopal Kumar, Yu-Chang Chan, Cheng-Wei Sun, Chih-Tung Chen

sediment flux monitoring for decadal timescales ($<10^1$ years) (Milliman & Farnsworth, 2011; Walling & Fang, 2003), cosmogenic radionuclide concentrations for millennial to million-year periods (10^3–10^6 years) (Granger et al., 2013; von Blanckenburg, 2006), and thermochronological methods for geological timescales exceeding 10^6 years (Ehlers & Farley, 2003; Reiners & Brandon, 2006). Several studies have attempted a comparison between short- and long-term rates within the same regions (Clapp et al., 2000; Gellis et al., 2004; Kemp et al., 2020; Kirchner et al., 2001; von Blanckenburg, 2006), but their findings exhibit substantial variability. Some studies report elevated short-term relative to long-term erosion rates (Gellis et al., 2004), while others document the inverse relationship (Kirchner et al., 2001).

Understanding temporal variations in erosion rates has become increasingly critical as anthropogenic climate change accelerates geomorphic processes globally (East & Sankey, 2020). Rising temperatures, glacial retreat, and intensifying extreme rainfall events have been linked to increased sediment export (Li, Lu, et al., 2021, Li, Huang et al., 2021; Micheletti & Lane, 2016; Prieur et al., 2025), yet the magnitude and direction of these changes remain site-specific and modulated by local feedbacks. With global warming accelerating and extreme event frequency increasing (Papalexiou & Montanari, 2019), determining whether contemporary erosion rates systematically exceed long-term background rates across diverse landscapes represents a fundamental question in Earth surface studies.

In mountainous environments, decadal-scale erosion rates are traditionally inferred from suspended sediment flux measurements (Andermann et al., 2012; Fuller et al., 2003; Li, 1976; Milliman & Farnsworth, 2011). While this approach provides valuable basin-scale erosion estimates, it presents certain methodological constraints that can compromise erosion rate quantification. First, suspended load measurements inherently overlook interim sediment storage, redistribution, and internal sediment migration within catchments, providing limited insight into spatial erosion heterogeneity and the buffering processes that regulate sediment delivery across scales. Second, accurate erosion quantification requires approximation of unmeasured bedload transport, introducing substantial uncertainty. Third, the quality of erosion estimates depends critically on sampling frequency and completeness, which can be compromised during extreme events due to instrument malfunction or failure (Dickinson, 1981; Fuller et al., 2003).

Advances in remote sensing can now provide independent erosion quantification through multi-temporal Digital Elevation Models (DEMs), offering a spatially explicit alternative (i.e., with erosion mapped at each location) to traditional flux-based approaches. These data sets, derived from radar, optical, or LiDAR sources (In Maune, 2007; Shean et al., 2016), enable direct measurement of elevation change and sediment volumes across tectonically active and climatically dynamic regions (Lin et al., 2020). DEMs of difference (DoD) facilitate cell-by-cell quantification of topographic change, providing volumetric erosion estimates that capture the full spectrum of geomorphic processes without the limitations inherent to sediment flux measurements. DoD approaches have been applied to monitor earthflows, landslides, debris flows, and other mass wasting processes (Brasington et al., 2012; Hsieh et al., 2016; Wheaton et al., 2010; Williams, 2012), but most research has relied on high-resolution LiDAR or photogrammetric DEMs, which restrict spatial coverage to relatively small areas. While LiDAR provides exceptional topographic accuracy, its recent emergence and high cost limit the availability of historical data for long-term assessments. Conversely, global satellite-derived DEMs offer broad spatial coverage and extended temporal baselines, though their potential for detecting decadal-scale topographic change remains underexploited due to inherent noise in these data sets (Purinton & Bookhagen, 2018). When the target geomorphic signal for detection is sufficiently large and appropriate correction methods are applied to address inherent errors and vegetation biases in global DEMs, genuine topographic change can be effectively isolated (Anderson, 2019; Nuth & Kääb, 2011; Wheaton et al., 2010).

Taiwan provides an ideal natural laboratory for such assessments, given its intense rainfall, rapid tectonic uplift, and frequent mass wasting events (Dadson et al., 2003; Tsou et al., 2011). Here, we evaluate decadal-scale land surface change in Taiwan's Laonong River Basin (Figure 1), a large mountainous drainage basin (1,373 km^2), to test whether recent erosion rates exceed long-term denudation rates estimated from cosmogenic and thermochronological approaches. We assess the suitability of several global elevation products, identify NASADEM as the most appropriate archival data set, and refine this DEM through vegetation bias correction and spectral filtering using high-resolution airborne LiDAR validation. Our integrated DoD approach enables spatially explicit erosion rate evaluation at both basin and sub-catchment scales, advancing our understanding of landscape adjustment to climatic perturbations in rapidly evolving mountainous environments.

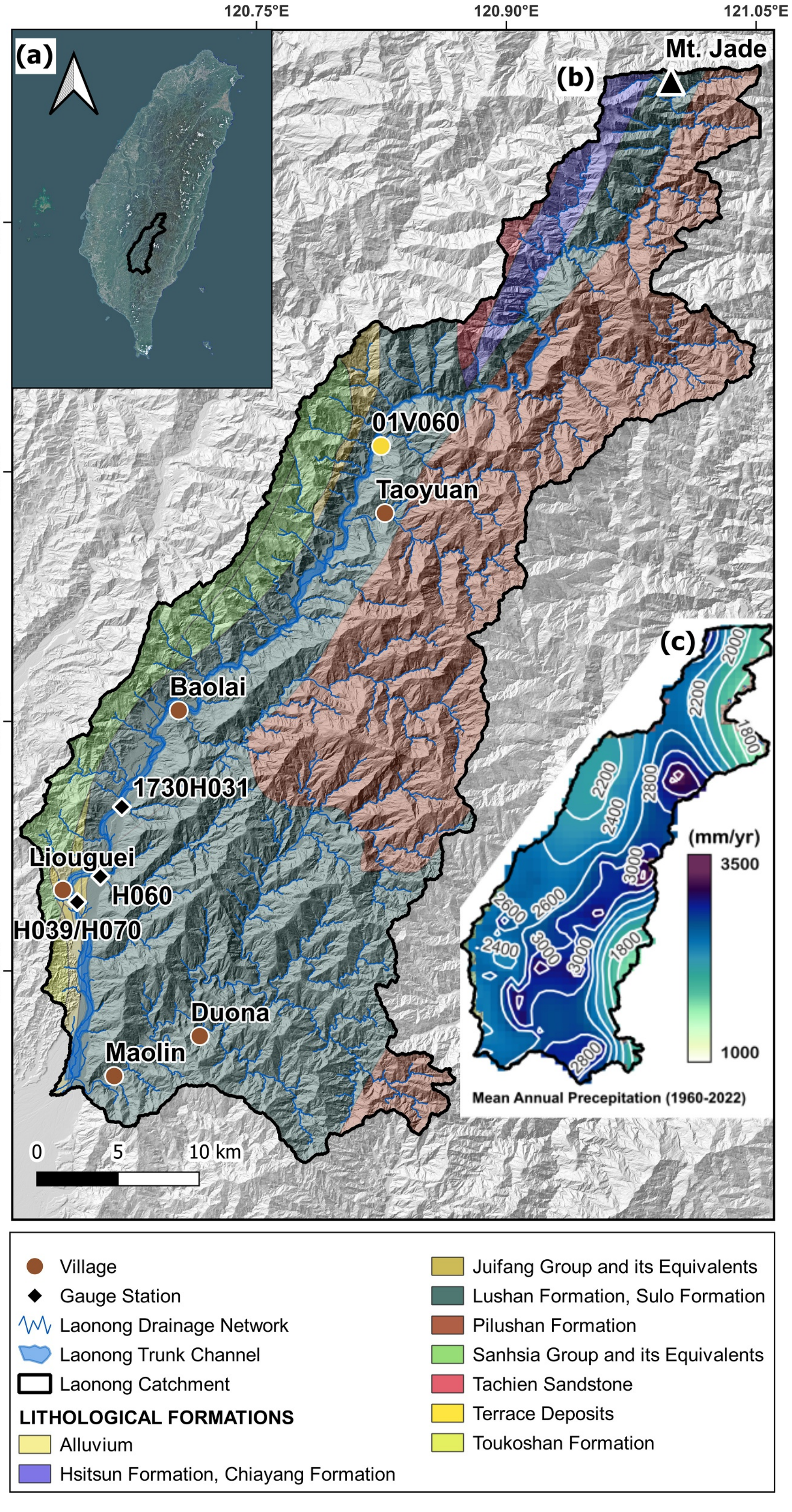
120.75°E
120.90°E
121.05°E
23.40°N
23.25°N
23.10°N
22.95°N
(a)
(b)
Mt. Jade
01V060
Taoyuan
Baolai
1730H031
Liouguei
H060
H039/H070
Duona
Maolin
0
5
10 km
(c)
(mm/yr)
3500
1000
Mean Annual Precepitation (1960-2022)
Village
Gauge Station
Laonong Drainage Network
Laonong Trunk Channel
Laonong Catchment
LITHOLOGICAL FORMATIONS
Alluvium
Hsitsun Formation, Chiayang Formation
Juifang Group and its Equivalents
Lushan Formation, Sulo Formation
Pilushan Formation
Sanhsia Group and its Equivalents
Tachien Sandstone
Terrace Deposits
Toukoshan Formation

Figure 1.

2. Study Area

The Laonong River Basin is located in southwestern Taiwan, draining the Central Mountain Range to the east and the Yushan Range to the west (Capart et al., 2010). The river originates near Mount Jade (Taiwan's highest peak at 3,952 m) and flows approximately 137 km southward before joining the Kaoping River (Weng et al., 2011). Elevations range from ∼130 m at the downstream boundary to over 3,600 m in the headwaters. The terrain is characterized by steep hillslopes (mean slope ∼35°) and widespread active landsliding, making it one of Taiwan's most geomorphically active catchments.

The basin is underlain predominantly by metamorphic rocks of the Central Range, including slate, phyllite, and argillite of the Lushan and Pilushan Formations, with lesser exposures of sandstone and conglomerate belonging to the Western Foothills (Hsitsun and Toukoshan Formations). Alluvial deposits and terrace sediments occur along the main channel corridor and at major tributary junctions. The weakly metamorphosed slate and phyllite are particularly prone to slope failure during intense rainfall (Weng et al., 2011).

The basin experiences a subtropical monsoon climate with pronounced seasonality. Mean annual precipitation (1960–2022) ranges from approximately 1,600 mm/yr in lower elevations to >3,500 mm/yr (Figure 1c), concentrated during the monsoon (May-September) and typhoon (June–October) seasons. Individual typhoons can deliver more than 1,000 mm within 24–48 hr (Weng et al., 2011). The 2000–2020 study period was anomalously wet, with mean annual precipitation exceeding the 1960–1999 baseline by 27% (Figure 2a). Typhoon Morakot (7–10 August 2009) was particularly extreme, delivering approximately 2,900 mm over three days and triggering thousands of landslides, including the catastrophic Putanpunas deep-seated landslide examined in this study (Tsou et al., 2011). Spatial precipitation data (1960–2022) were obtained from the Taiwan Climate Change Projection Information and Adaptation Knowledge Platform (TCCIP) at 0.01° resolution, integrating measurements from the Water Resources Agency (WRA) and Central Weather Administration network stations (Lin et al., 2022). Daily rainfall records from WRA station 01V060, located within the basin, provide a continuous record of extreme events during the study period (Figure 2b). Water discharge and suspended sediment concentration were monitored at gauging stations along the main channel throughout the study period (Figure 3).

3. Materials and Methods

3.1. Data Sources and Datum Homogenization

This study utilized two primary sources of elevation data. The reference data set consisted of a 20 m LiDAR DEM released in 2020 with acquisition periods ranging from 2016 to 2020 (hereafter termed as 2020 LiDAR DEM), which was used as the benchmark due to its superior vertical accuracy. This data set represents a downsampled version of Taiwan's national 1-m resolution LiDAR DEM, which demonstrates reported vertical accuracy of less than 0.3 m (Chen et al., 2015). The second data set included a set of freely available, satellite-derived global DEMs, including TanDEM-X EDEM, Copernicus DEM, ALOS World 3D DEM (AW3D30), ASTER GDEM, SRTM DEM, FABDEM, and NASADEM (Table 1). We excluded MERIT DEM from our analysis as its 90-m resolution limits detection of tributary-scale sediment dynamics and channel-level geomorphic changes. While coarser DEMs may suffice for capturing broad patterns of mass redistribution, our sub-catchment analysis requires resolution capable of detecting features such as tributary channels (40–50 m wide) and smaller landslides.

To ensure accurate intercomparison between data sets, all DEMs were projected to WGS84 and horizontally coregistered to sub-pixel accuracy based on systematic relationships between slope, aspect, and apparent change in areas assumed to be stable between surveys (Nuth & Kääb, 2011). Vertical consistency was ensured by referencing all data sets to the EGM2008 geoid, which provides improved accuracy compared to EGM96 (Üstün et al., 2016). Global DEMs originally referenced to EGM96 were transformed to EGM2008 by applying the geoid

Figure 1. Geographic location, geological setting, and precipitation patterns of the study area. (a) Orthoimage of Taiwan Island; the black polygon highlights the location of the Laonong River Basin within Taiwan. (b) Enlarged map of the Laonong River Basin showing major villages (brown dots), downstream gauge stations (black diamonds), the rainfall station used for the time series in Figure 2 (yellow dot), and the underlying lithological units. (c) Spatial distribution of mean annual precipitation (1960–2022), derived from high-resolution gridded precipitation data (0.01°) provided by the Taiwan Climate Change Projection Information and Adaptation Knowledge Platform (TCCIP). This data set integrates rainfall measurements from multiple weather station networks, including the Water Resources Agency and Central Weather Administration stations (Lin et al., 2022).

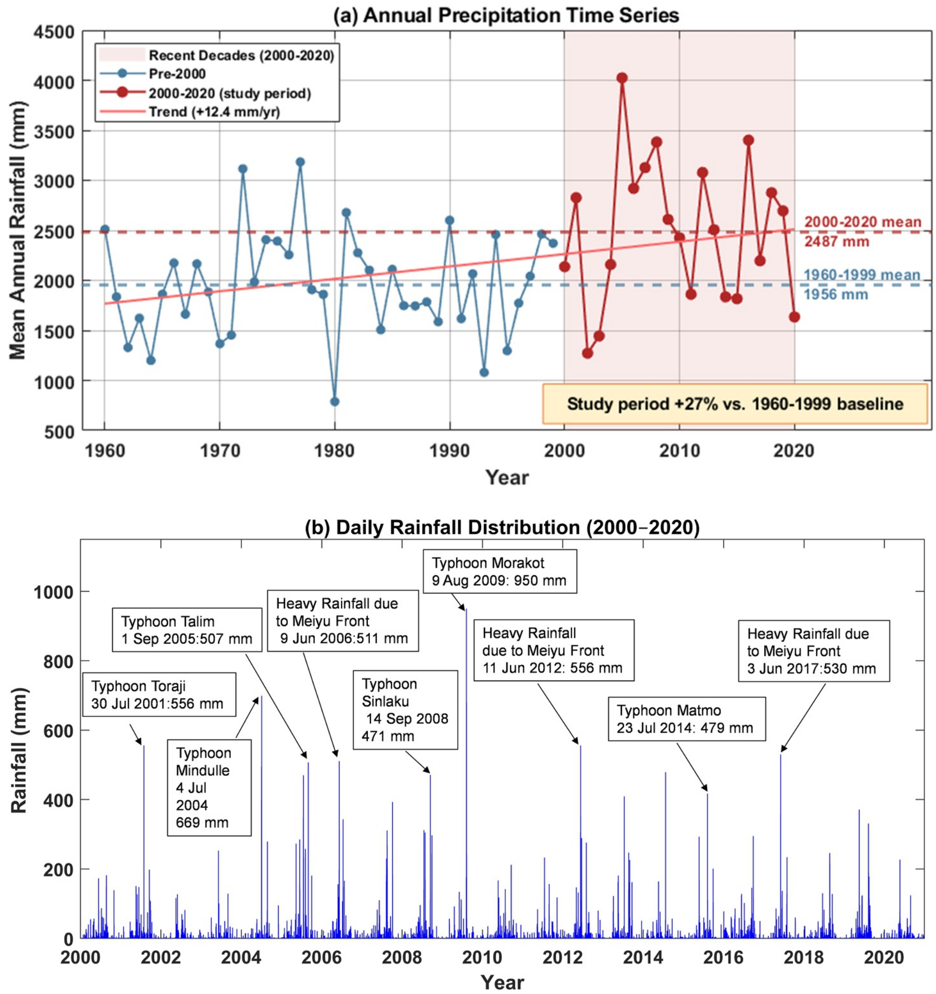

Figure 2. (a) Mean annual precipitation in the Laonong River Basin (1960–2020) derived from gridded rainfall data (TCCIP; 0.01° resolution). The study period (2000–2020, shaded) averaged 2,487 mm, representing a 27% increase relative to the 1960–1999 baseline (1,956 mm). Dashed horizontal lines indicate period means. The positive trend (+12.4 mm/yr) reflects increasing precipitation over recent decades, consistent with intensifying extreme rainfall events across Taiwan (Henny et al., 2021). (b) Daily rainfall time series from station 01V060 maintained by the Water Resources Agency, Taiwan, for the period 2000–2020. Typhoon-related and torrential rain events affecting the study area are indicated. The record includes multiple extremes, with maximum daily totals up to 950 mm.

height difference between EGM96 and EGM2008 (Okolie et al., 2024), while the LiDAR DEM, referenced to the local TWHyGEO2014 geoid, was referenced to EGM2008 using the difference between EGM2008 and TWHyGEO2014 (National Land Surveying and Mapping Center, Taiwan). Full details of the vertical datum transformation are provided in Supporting Section Text S1 and Figure S1 in Supporting Information S1.

3.2. DEM Selection and Evaluation

A three-step analysis was conducted to evaluate the consistency, accuracy, and noise characteristics of DEMs to make an informed decision about choosing the most suitable global DEM for topographic change detection (Figure 4).

3.2.1. Accuracy Assessment Using Stable Areas in the Spatial Domain

The vertical accuracy of each DEM was assessed in geomorphically stable regions where both elevation and land cover remained unchanged throughout the recent decades. Given that DEMs such as SRTM (February 2000), Copernicus DEM (2010–2015), and FABDEM (2010–2015) were acquired across different decades, only pixels

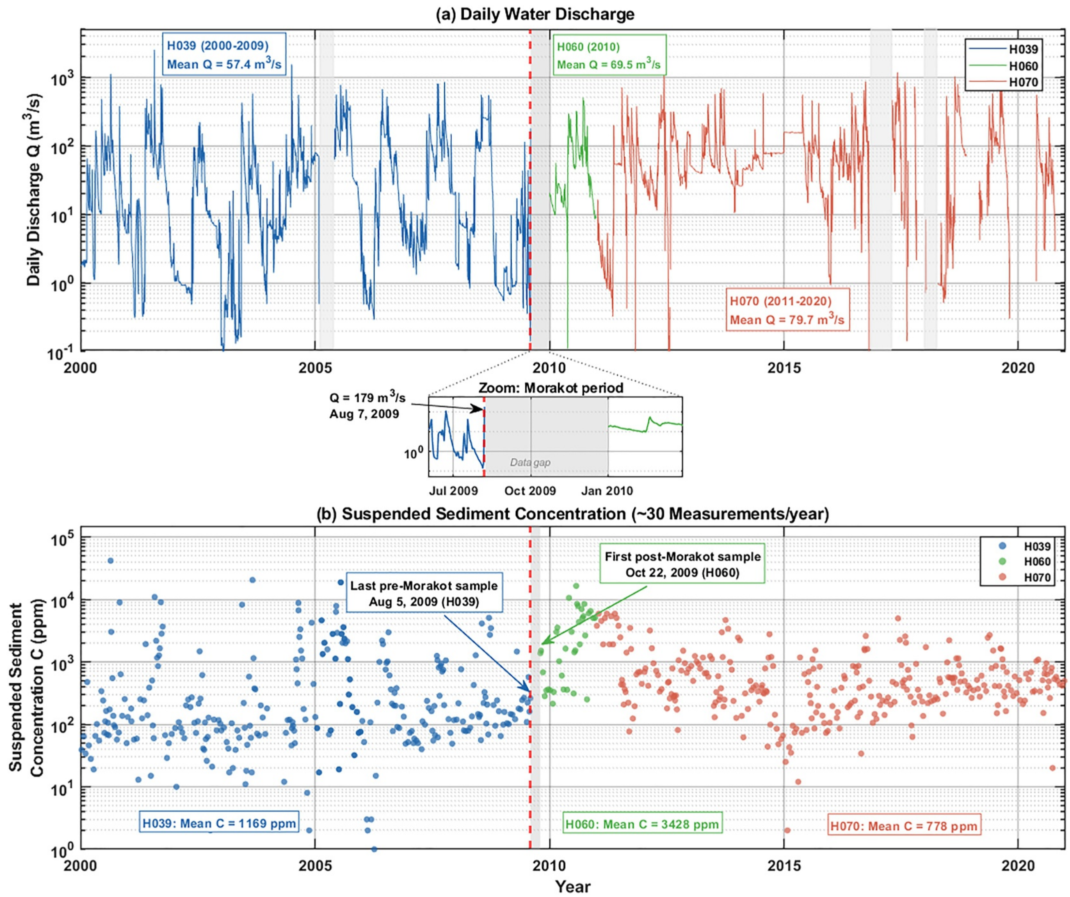

Figure 3. Time series of (a) daily water discharge and (b) suspended sediment concentration at gauge stations in the Laonong River Basin, 2000–2020. Station H039 (blue) provides measurements from 2000 until its destruction by Typhoon Morakot in August 2009 (red dashed line). Following Morakot, measurements resumed at nearby station H060 (green, 2010) before transitioning to station H070 (red, 2011–2020) at the same location. The inset in (a) shows the Morakot period in detail, with the data gap indicating station destruction. Gray shading highlights other temporal gaps in continuous water discharge data. Note the elevated mean suspended sediment concentration at H060 (3,428 ppm) immediately following Morakot compared to pre-event conditions at H039 (1,169 ppm), reflecting abundant landslide-derived sediment supply. Drainage areas: H039/H070 = 885 km^2; H060 = 870 km^2. The sediment sampling frequency is approximately 30 measurements per year.

Table 1
List of Free Available Satellite-Derived Global Digital Elevation Model Data Sets Evaluated in the Study

DEM name	Horizontal datum	Vertical datum	Coverage	Acquisition method	Data acquisition period	Recent version release year
SRTM V3	WGS84	EGM96	Nearly Global (60°N to 56°S)	Radar (SRTM mission)	February 2000	September 2014
NASADEM	WGS84	EGM96	Nearly Global (60°N to 56°S)	Radar (SRTM mission)	February 2000	2020
ASTER GDEM V3	WGS84	EGM96	Nearly global (83°N to 83°S)	Optical (ASTER)	2000–2013	2019
Copernicus DEM	WGS84	EGM2008	Global	Radar (TanDEM-X, TerraSAR-X)	2010–2015	2024
TanDEM-X EDEM	WGS84	EGM2008	Global	Radar (TanDEM-X, TerraSAR-X)	2010–2014	2023
ALOS World 3D (AW3D30)	WGS84	EGM96	Nearly global (82°N to 82°S)	Optical (ALOS PRISM)	2006–2011	2024
FABDEM	WGS84	EGM2008	Global	Derived from Copernicus DEM	2010–2015	2023

Note. References: Tadono et al. (2014), LP DAAC (2019), Airbus (2020), NASA JPL (2020), González et al. (2020), Japan Aerospace Exploration Agency (2021), Uhe et al. (2022), European Space Agency (2024).

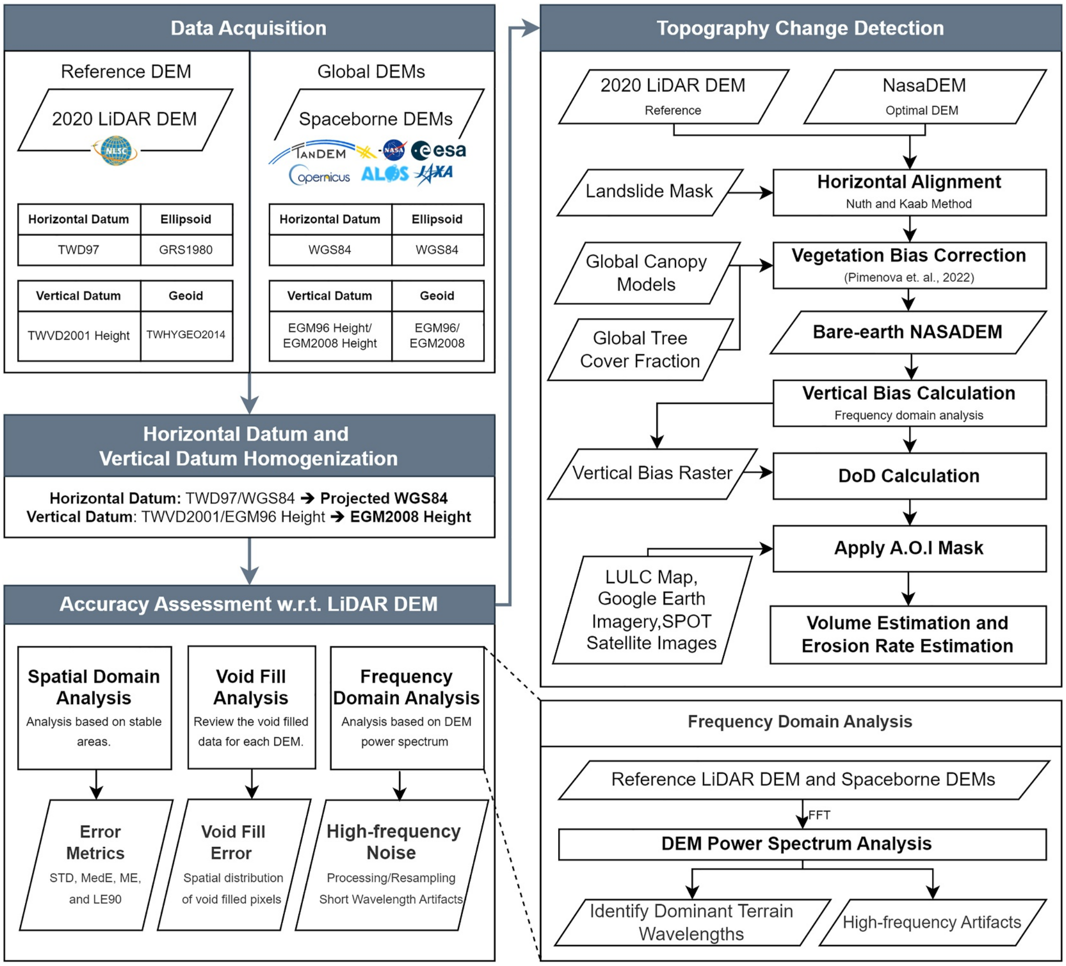

Figure 4. Workflow for digital elevation model (DEM) selection and sediment-volume estimation. Left: preprocessing and evaluation applied to the global DEMs to identify the data set most suitable for sediment-volume calculations. Right: steps for quantifying sediment volume from the selected DEM, including co-registration, vegetation bias correction, vertical referencing, DEM differencing, and integration of erosion and deposition volumes. Bottom right: frequency-domain analysis (2-D Fourier transform) used to detect high-frequency artifacts and identify dominant wavelengths; the resulting low-pass surface approximates stable topography for vertical-bias estimation prior to computing the final DEMs of difference.

without significant elevation changes and with stable land use and land cover were chosen for accuracy assessment. The selected test polygons were primarily high, flat terraces located away from river channels and mountain fronts, ensuring they had not been influenced by landslides, slope failures, or debris flows over the past decades (Figure S2 in Supporting Information S1). Of the 55 identified stable polygons, 52 lie within the Laonong Basin and three lie near the downstream outlet. Fan terraces were specifically excluded due to potential modification by sediment influx from extreme geomorphic events such as typhoons and torrential rainfall events. Site stability was validated using high-resolution landslide inventories from Taiwan's National SPOT satellite images mapping landslides annually from 2001 to 2015 (GSMMA, 2023), historical Google Earth imagery (Google Earth Pro, 2024), and high-resolution SPOT satellite images annually from the Center for Space and Remote Sensing Research, National Central University, Taiwan (CSRSR, 2024). These data sets revealed regions where true elevation change was negligible, and we used these regions for DEM evaluation against the LiDAR reference.

3.2.2. Void-Filled DEM Assessment and Inconsistencies in Multi-Temporal Analysis

Void-filled regions in each DEM were mapped to identify areas where external data sources or interpolation may compromise elevation accuracy for multi-temporal analysis. When elevation data from external sources are used to fill voids caused by radar shadowing or cloud cover, two issues arise: temporal mismatches between void-fill

10.1029/2025JF008720

data and primary DEM acquisition dates, and accuracy variations from data sets of differing resolution and quality (Marešová et al., 2024; Tachikawa et al., 2011).

To assess the void-fill extent, product-specific metadata layers were examined for each DEM. The SRTM and NASADEM NUM layers indicate pixels filled using GMTED2010 or ASTER; Copernicus DEM and TanDEM-X provide confidence layers and height-error maps; ASTER GDEM includes mask layers identifying interpolated pixels (Gesch et al., 2016; Mesa-Mingorance & Ariza-López, 2020). Spatial distributions of void-filled pixels were mapped across the study area to compare reliance on external data sources among DEMs. To reduce the likelihood of spurious elevation signals in the final DoD, DEMs with minimal void-filling were prioritized for this study.

3.2.3. DEM Quality Assessment in the Frequency Domain

Frequency domain analysis using the Fourier transformation was employed to evaluate how well each DEM represented terrain features across multiple spatial scales, complementing conventional pixel-wise differencing for accuracy assessment. This analysis identified high-frequency noise and processing artifacts in global DEMs that could compromise change detection accuracy. Following established methodologies in DEM spectral analysis (Booth et al., 2009; Perron et al., 2008; Purinton & Bookhagen, 2017), two-dimensional Fast Fourier Transformation (FFT) was applied to decompose each DEM into its constituent frequency components, allowing identification of systematic distortions not apparent in pixel-level comparisons (Arrell et al., 2008; Purinton & Bookhagen, 2017, 2018). A 2-D Discrete Fourier Transform was performed on each DEM subset, converting spatial elevation data into the frequency domain (for details, see Kumar et al. (2024), Sect. 4.2). The resulting 2D power spectra were then radially averaged, producing a one-dimensional representation of wavelengths (or radial frequencies) versus mean-squared amplitude. This spectral decomposition enables a clear distinction between long-wavelength components (low-frequency) corresponding to broad geomorphic structures such as major ridgelines and valley networks, and short-wavelength components (high-frequency) revealing fine-scale terrain features, processing artifacts, or sensor-related noise. Spectral peaks detected at high frequencies in the global DEMs, which were not observed in the corresponding LiDAR data sets, were interpreted as processing artifacts or surface features that do not accurately represent bare-earth terrain conditions (Kumar et al., 2024).

DEM selection was based on the three complementary criteria derived from the preceding analyses, that is, vertical accuracy in stable areas, void-fill extent from product metadata, and spectral noise characteristics evaluated via FFT analysis. The optimal DEM for multi-temporal change detection was defined as having minimal high-frequency artifacts, limited external void-filling, and low systematic bias relative to LiDAR. This DEM was then used for DoD generation following the workflow in Figure 4. Application of these criteria identified NASADEM as the optimal DEM (evaluation details in Section 4.2). The following sections describe bias corrections specific to this data set prior to DoD generation.

3.3. Vegetation Bias and Vertical Bias Correction

The selected DEM required correction for two systematic biases to transform the global DSM into a bare-earth DEM suitable for change detection: (a) vegetation bias from canopy returns in SRTM C-band radar, and (b) vertical bias relative to LiDAR.

To derive a bare-earth digital terrain model for the year 2000, we implemented the vegetation bias correction model proposed by Pimenova et al. (2022). We first reconstructed a canopy height model for the year 2000 (CHM2000) by combining the Global Forest Canopy Height (GFCH2019) data set from 2019, the Hansen Global Forest Change tree-cover product for the year 2000, and the Forest Canopy Height Map from 2005. This reconstruction was achieved through a rule-based classification of pixels into clearing, growth, and no-change categories. Vegetation bias was then estimated using the equation $\mathrm{VB} = \mathrm{a} \times \mathrm{CHM2000} \times \rho$, where ρ represents the canopy density fraction and $a = 0.585$ represents an empirically derived scaling coefficient from Pimenova et al. (2022) optimized for NASADEM correction, which incorporates the effects of C-band radar penetration characteristics. Further details regarding the vegetation bias correction workflow are provided in Figures S2–S4 in Supporting Information S1. The resulting vegetation bias layer was subtracted from the original NASADEM to produce a vegetation-corrected, bare-earth terrain surface suitable for geomorphic analysis.

Following vegetation bias removal, systematic vertical offsets were corrected using frequency-selective filtering. This approach is particularly valuable in our study area because stable-area based methods, while remaining the established standard for DEM co-registration and bias correction (Anderson, 2019; Besl & McKay, 1992; Chen & Medioni, 1992; Hugonnet et al., 2022; Nuth & Kääb, 2011; Rosenholm & Torlegård, 1988; Shean et al., 2016) face challenges in landscapes where stable ground is scarce or poorly distributed, a condition characteristic of tectonically active, typhoon-affected Taiwan. The theoretical foundation for this approach is established in geomorphological spectral analysis, where Perron et al. (2008) demonstrated that characteristic wavelengths of first-order landscape organization can be objectively identified through power spectral scaling relationships. Quasi-periodic ridge-valley structures emerging from uniform erosional processes produce distinct spectral signatures at characteristic spatial wavelengths, providing a physical basis for frequency-selective filtering. In DEM analysis, low-pass filtering suppresses short-wavelength components while retaining long-wavelength components that describe broader topographic features (Grieve et al., 2016; Lindsay et al., 2019).

A Gaussian low-pass filter was applied to the vegetation bias corrected NASADEM to extract broad-scale ridge and valley structures corresponding to dominant spectral peaks that reflect landscape components unchanged over decadal timescales. An identically filtered LiDAR DEM served as the reference for differencing analysis, where persistent discrepancies indicate systematic vertical biases, as these long-wavelength topographic components should remain consistent between DEMs over decadal timescales. The difference bias raster between filtered surfaces represents systematic vertical bias, which was subtracted from the NASADEM to produce the final co-registered, bias-corrected archival DEM.

3.4. Sediment Volume/Erosion Rate Estimation and Uncertainty Analysis

The corrected DoD map was calculated by subtracting the co-registered and bias-corrected NASADEM from the LiDAR DEM. Pixels with persistent vegetation cover in both DEMs were masked using the ESRI Sentinel-2 10 m Land Use/Land Cover data set to exclude high-uncertainty areas from volumetric calculations. The effective analysis area after masking comprises approximately 105 km^2. We assume a negligible net change in the excluded forested areas.

The total erosional and depositional volumes were computed by summing the product of pixel area and elevation differences for all negative and positive pixels in the DoD map, respectively. The exported volume was determined as the difference between erosion and deposition volumes:

$$V_{ex} = V_e - V_d = A\left(\sum_{i=1}^{N} \Delta Z_i\right) \tag{1}$$

where V_{ex} is exported volume, V_e is eroded volume, V_d is deposited volume, A is pixel area, and ΔZ_i represents the elevation change of the ith pixel across all n pixels with elevation changes. To derive sediment erosion rates, the exported volume was normalized by the catchment area and time interval between DEM acquisitions:

$$\frac{dz}{dt} = \frac{V_{ex}}{A_b \Delta T} \tag{2}$$

where dz/dt is the erosion rate (mm/year), V_{ex} is the total exported volume, A_b is the basin area, and ΔT is the time interval between DEMs.

We incorporate error modeling for volumetric uncertainty following Anderson (2019) and Schwat et al. (2023), with an additional term to account for uncertainty in vegetation bias correction. Following Anderson (2019), who demonstrated that random errors systematically bias gross change estimates but cancel in net change calculations, we report thresholded gross erosion and deposition alongside unthresholded net change. Gross values include only pixels exceeding a level of detection threshold of ±1.82 m (95% confidence interval, $1.96 \times \sigma\_rms$; Table 2), while net change and associated uncertainties are computed for all analyzable pixels using error propagation methods to define uncertainty bounds.

The total volumetric uncertainty combines four independent error sources and is expressed as:

Table 2
Estimation of Different Error Components for the Corrected and Uncorrected Digital Elevation Models of Difference, Followed After Anderson, 2019; Schwat et al., 2023

Parameter	Uncorrected DoD	Corrected DoD
σ_{rms} (m)	2.49	0.93
σ_{sc} (m)	0.97	0.86
a_{i} (m)	114.25	107.88
σ_{sys} (m)	1.78	0.11
σ_{VB} (m)	–	1.26
$\sigma_{\{v_{\{\mathrm{total}\}}\}}$ (m^3)	186,799,624.30	43,951,185.60

Note. After correcting for the vegetation bias and vertical bias in the Fourier domain, there is a significant reduction in all the error components.

$$\sigma_{\{v_{\{\mathrm{total}\}}\}} = \sqrt{\left\{\sigma^2_{\{v,R\}} + \sigma^2_{\{v,\mathrm{sc}\}} + \sigma^2_{\{v,\mathrm{sys}\}} + \sigma^2_{\{v,\mathrm{veg}\}}\right\}} \tag{3}$$

Where $\sigma_{\{v,R\}}$, $\sigma_{\{v,\mathrm{sc}\}}$, $\sigma_{\{v,\mathrm{sys}\}}$ and $\sigma_{\{v,\mathrm{veg}\}}$ represent volumetric uncertainties arising from uncorrelated random errors, spatially correlated random errors, systematic errors, and vegetation bias correction, respectively. The first three components are calculated as

$$\sigma_{v,R} = \sqrt{n}L^2\sigma_{\mathrm{rms}} \tag{4}$$

$$\sigma_{v,\mathrm{sc}} = 0.79\ a_i\sqrt{n}L\ \sigma_{\mathrm{sc}} \tag{5}$$

$$\sigma_{v,\mathrm{sys}} = n\ L^2\sigma_{\mathrm{sys}} \tag{6}$$

where, n is the number of DoD cells excluding persistently vegetated pixels, L is the cell dimension, σ_{rms} is the root mean square of vertical errors, a_{i} is the range of the semi-variogram describing spatial correlation, σ_{sc} is the standard deviation of spatially correlated errors (estimated from the square root of semi-variance at the sill), and σ_{sys} is the systematic vertical error. Random samples from identified stable areas were used to compute the root mean square error (RMSE) and the mean for uncorrelated random error and systematic error estimation, respectively. To determine the spatially correlated error, we employed the methodology outlined by Anderson (2019) and East et al. (2021). The spatially correlated error was estimated using semivariogram analysis, performed via the kriging tool in ESRI ArcMap's Geostatistical Analyst extension. A spherical semivariogram model with no nugget was fitted to the empirical semivariogram of DoD values over stable areas, following Anderson (2019) and Rolstad et al. (2009).

The vegetation bias correction introduces an additional source of uncertainty through the empirically derived scaling coefficient ($a = 0.585$) in the formulation VB = a × CHM × ρ. While this coefficient falls within the established range of 0.5–0.6 supported across diverse forest environments (Carabajal & Harding, 2005; O'Loughlin et al., 2016; Su et al., 2015), the uncertainty associated with this parameter must be propagated through the volumetric calculations. The vegetation-related volumetric uncertainty is calculated as

$$\sigma_{v,\mathrm{veg}} = n_{\mathrm{veg}}\ L^2\sigma_{\mathrm{VB}} \tag{7}$$

where n_{veg} is the number of pixels requiring vegetation bias correction and σ_{VB} is the per-pixel uncertainty in vegetation bias, estimated as:

$$\sigma_{\mathrm{VB}} = \Delta a \times \overline{\mathrm{CHM} \times \rho} \tag{8}$$

Here, $\Delta a = 0.1$ represents the range of plausible correction coefficients (0.5–0.6), and $\overline{\mathrm{CHM} \times \rho}$ is the mean product of canopy height and canopy density fraction across corrected vegetated pixels. Vegetation cover in 2,000 was identified using the Hansen Global Forest Change tree cover data set (Hansen et al., 2013), classifying pixels as vegetated where fractional tree cover exceeded a threshold of 0.25 (Tyukavina et al., 2015). Only these pixels, which received vegetation bias correction, were included in the n_{veg} count for Equation 7. By propagating uncertainties from each independent error source through the volume calculation, this framework provides quantitative confidence bounds on the net sediment volume estimates reported in Section 4.3.

3.5. Suspended-Sediment Derived Erosion Rates From Rating-Curve Analysis

Suspended sediment concentration and discharge data were obtained from the WRA, Ministry of Economic Affairs, Taiwan. The WRA conducts routine and event-based sediment sampling at more than 250 hydrological stations across Taiwan, providing dense sediment monitoring networks in the region (Kao & Milliman, 2008). Suspended sediment concentration is determined using DH-48 depth-integrated samplers at gauging stations (Kao et al., 2005). These data have been widely employed in previous sediment budget and denudation studies in Taiwan (Dadson et al., 2003, 2004; Kao & Milliman, 2008; Li et al., 2005; Ruetenik et al., 2024).

Suspended-sediment derived erosion rates were estimated following the rating-curve methodology commonly applied to rivers in Taiwan (Li et al., 2005). This approach relates suspended sediment concentration to water discharge through an empirical power-law relationship, enabling reconstruction of continuous sediment flux time series from discrete sampling data.

Suspended sediment concentration C (mg L^{-1}) is related to water discharge Q (m^3 s^{-1}) by a power-law relationship (Asselman, 2000; Ferguson, 1986):

$$C = a \cdot Q^b \tag{9}$$

where a and b are empirically derived coefficients. Instantaneous suspended sediment load Q_s (t day^{-1}) is calculated as

$$Q_s = k \cdot C \cdot Q \tag{10}$$

where $k = 0.0864$ is the unit-conversion factor. Combining Equations 9 and 10 yields the suspended sediment rating curve:

$$Q_s = A \cdot Q^B \tag{11}$$

where $A = k \cdot a$ and $B = b + 1$. For each gauging station, coefficients were estimated by ordinary least-squares regression in log-log space using paired spot measurements of suspended sediment concentration and discharge (Li et al., 2005).

The fitted rating curves were applied to daily discharge records to reconstruct a daily time series of suspended sediment load for the period 2000–2020, with station-specific sub-periods determined by data availability. Daily suspended loads were summed to obtain annual suspended sediment mass M_y (t yr^{-1}), and the mean annual suspended sediment mass $\bar{M}$ was calculated by averaging annual totals across the available years. Mean annual sediment mass was converted to volumetric sediment transport rate V (Mm^3 yr^{-1}) assuming a bulk sediment density $\rho = 2.6 \times 10^3$ kg m^{-3} (Fuller et al., 2003):

$$V = \left(\overline{M} \times 1000\right) / \left(\rho \times 10^6\right) \tag{12}$$

Basin-averaged suspended-sediment erosion (denudation) rate E (mm yr^{-1}) was then calculated by normalizing sediment volume by upstream drainage area A_b (km^2):

$$E = (V/A_b) \times 1000 \tag{13}$$

4. Results

4.1. DEM Quality Assessment

4.1.1. Accuracy Results Based on Spatial Analysis of Stable Areas

The stable-area vertical accuracy assessment revealed distinct performance differences among the global DEMs (Figure 5). FABDEM demonstrated the smallest bias (median error ≈ -0.40 m) (Figure 5c), while AW3D30 showed the lowest variability (STD $\approx$ 1.09 m) (Figure 5b) despite a slightly higher positive bias ($\approx$0.94 m) (Figure 5a). Copernicus DEM and TanDEM-X consistently overestimated elevations (median errors >2.5 m) but exhibited narrow interquartile ranges (Figure 5c), indicating systematic rather than random bias. ASTER exhibited the poorest performance (Figures 5a–5d) with significant underestimation (median error ≈ -1.4 m) and the highest variability (STD $\approx$ 2.91 m). SRTM and NASADEM showed intermediate performance with moderate bias and variability. All statistical metrics (ME, MedE, IQR, LE90) showed agreement in ranking DEM performance and are summarized in Figure 5.

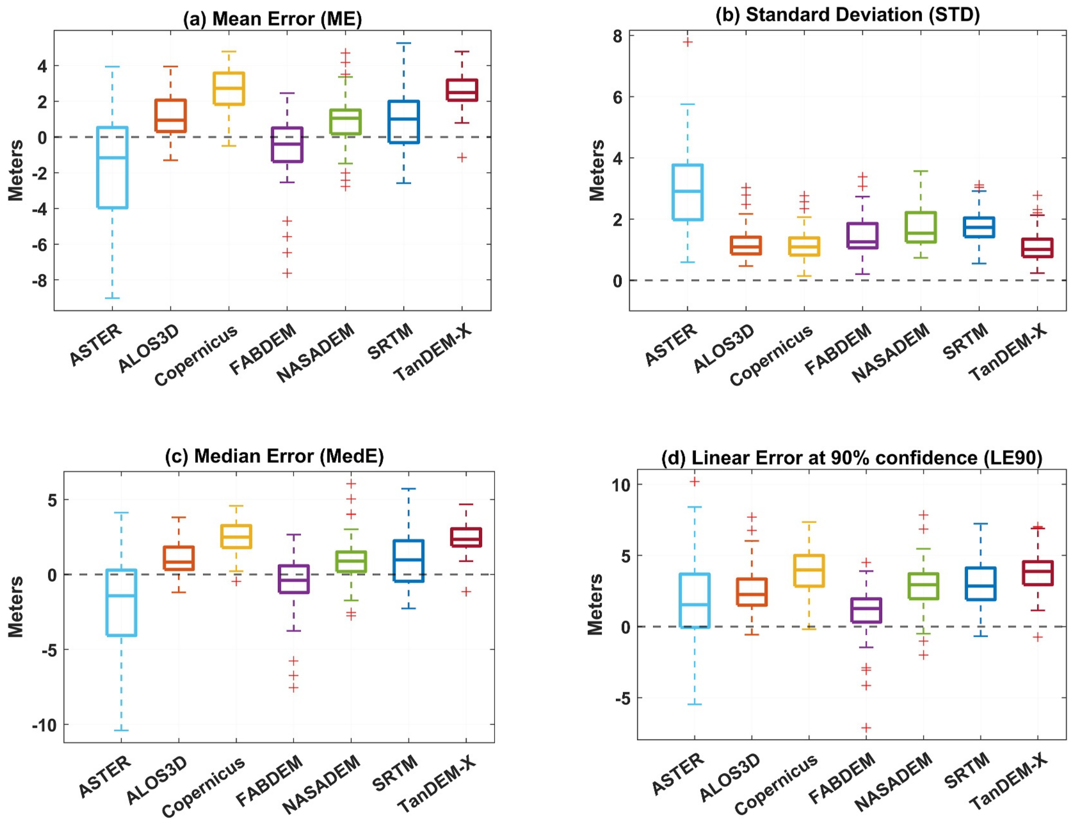

Figure 5. Box plot representation summarizing vertical accuracy metrics for each digital elevation model (DEM) across 55 stable reference polygons. Each box illustrates the distribution of mean error, median error, standard deviation, and LE90 values calculated individually from polygon-based differences against the reference LiDAR DEM. The horizontal line inside each box indicates the median value, while the boxes represent values within the interquartile range (from the 25th to the 75th percentiles). Whiskers extend to values within 1.5 times the interquartile range from the box edges, and data points beyond this range, marked by red plus signs, represent outliers. ASTER GDEM notably exhibits large variability across all metrics, indicating its lower reliability and consistency compared to the other DEMs evaluated.

4.1.2. Void Artifacts Assessment

Void-filled pixel distribution varies systematically with terrain and land cover (Figure 6). Radar-derived DEMs show concentrated void-filling in upstream forested areas and steep terrain where radar shadowing limits coverage (Figures 6d–6f). TanDEM-X EDEM exhibits extensive corrections, primarily in upper watershed regions associated with systematic drift adjustment (Figure 6e). In contrast, optically derived DEMs (ASTER GDEM, ALOS World 3D) show minimal external void-filling but rely on multi-temporal aggregation that may introduce temporal inconsistencies (Figures 6a and 6b). Across all DEMs, upstream and heavily forested portions show the highest void-fill concentrations, reflecting persistent acquisition challenges in these environments.

4.1.3. Spectral Analysis of DEMs in the Frequency Domain

Power spectral density analysis reveals fundamental differences in terrain representation between optical and radar-derived DEMs (Figures 7 and 8). Optical DEMs exhibit pronounced high-frequency noise contamination, with ALOS World 3D displaying spectral peaks around 60 m, corresponding to 2-pixel steps and extending through wavelengths up to 240 m (Figure 7). This broad spectral contamination indicates vulnerability to sensor noise, stereo-matching errors, and downsampling effects, overlapping with characteristic dimensions of hillslope processes including shallow landslides, debris flows, and gully systems (Marc & Hovius, 2015; Roering et al., 1999). ASTER GDEM demonstrates similar but less pronounced spectral peaks at ~60 m, suggesting vertical inaccuracies arising from inconsistencies in multi-stereo image pair fusion (Gesch et al., 2016). Radar-derived DEMs demonstrate superior spectral characteristics with smoother power spectra and substantially reduced high-frequency noise (Figure 8). Copernicus DEM and NASADEM exhibit smooth spectral curves

10.1029/2025JF008720

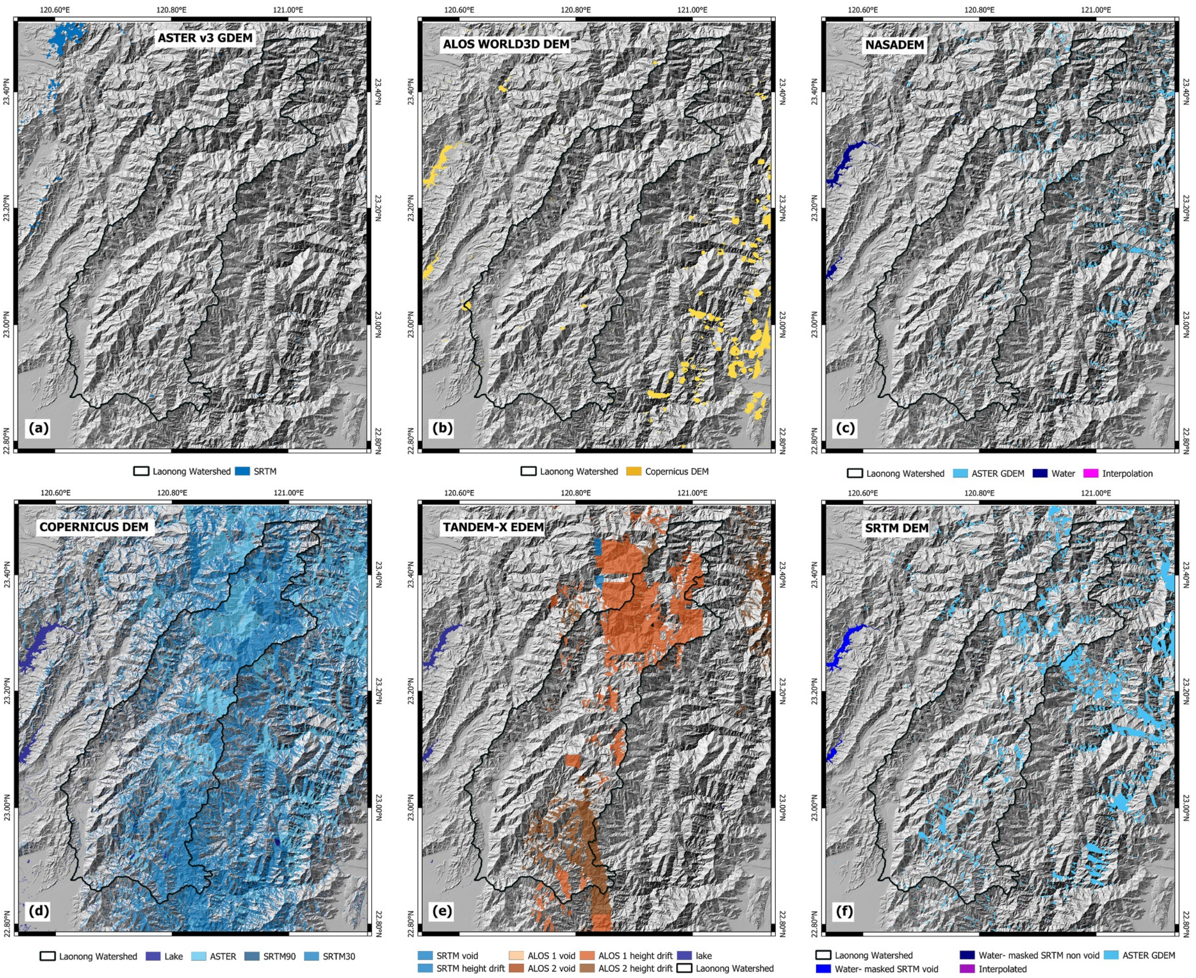

Figure 6. Spatial distribution of void-filled pixels and auxiliary data sourced from external digital elevation models (DEMs), overlaid on a hillshade background, for (a) ASTER GDEM, (b) ALOS DEM, (c) NASADEM, (d) Copernicus DEM, (e) TanDEM-X EDEM, and (f) SRTM DEM. Highlighted pixels represent areas where original elevation data gaps were filled using secondary sources, indicating regions of potential uncertainty and reduced vertical accuracy. Despite its excellent vertical accuracy, (d) Copernicus DEM is less suitable for multitemporal analysis in the study area due to extensive void-filling from external data sets. Conversely, (a)–(c) ASTER GDEM, ALOS DEM, and NASADEM exhibit significantly less reliance on external void-filling.

effectively suppressing short-wavelength artifacts through improved interferometric processing chains and high-quality void-filling procedures (Crippen et al., 2016; Guth & Geoffroy, 2021). TanDEM-X shows minimal spectral power increases at short wavelengths, reflecting effective speckle suppression through rigorous calibration and multi-baseline averaging (Wessel, 2018). SRTM displays subtle high-frequency noise increases consistent with known orbital striping errors from mast vibration and baseline fluctuations (Purinton & Bookhagen, 2021; Van Zyl, 2001), while FABDEM contains distinct artifacts at similar wavelengths likely due to interpolation and external data set fusion processes.

Power spectral analysis identified two dominant topographic wavelengths in the study area, that is, 2.8 and 1.3 km (Figures 7 and 8). Band-pass filtering of frequency components associated with these wavelengths and inverse Fourier transformation to the spatial domain confirmed that the 2.8 km wavelength corresponds to the major ridge-valley structure, while the 1.3 km wavelength represents tributary valley spacing orthogonal to the primary drainage network. These dominant peaks confirm that spectral analysis effectively captures natural landscape spatial organization, validating the frequency domain approach for terrain characterization. Low-pass filtering at the 2.8 km threshold preserves large-scale topographic features while enabling quantitative assessment of vertical biases through comparison with similarly filtered LiDAR reference data.

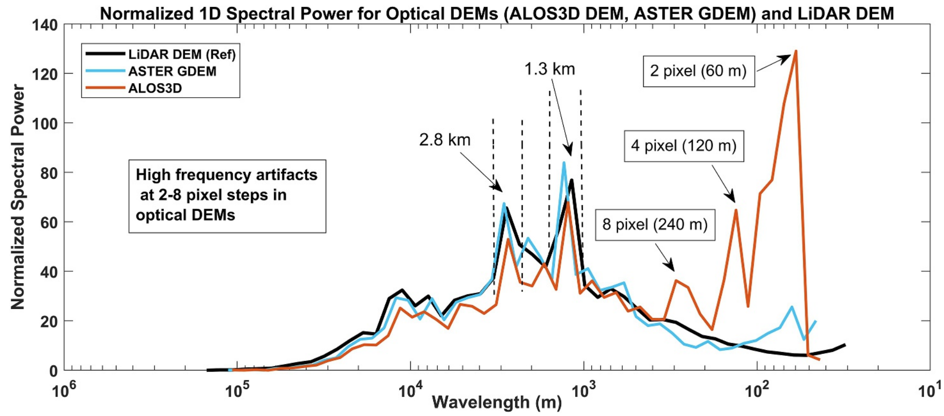

Figure 7. Normalized one-dimensional power spectra envelope for different optical digital elevation models (DEMs) evaluated in the study. Each envelope represents the 99.99th percentile of normalized spectral power computed from 2D FFTs of DEM tiles that were radially averaged into 1D spectra. Spectra were normalized by a fitted power-law background to highlight dominant terrain wavelengths. The percentile envelopes were derived from 20 logarithmically spaced wavelength bins to isolate low-frequency (long-wavelength) terrain components (after Purinton & Bookhagen, 2017). High-frequency peaks were observed at 2–8 pixel intervals in the optical DEMs, with similar artifacts previously reported in the AW3D5 and ALOS 3D DEMs by Purinton and Bookhagen (2017) and Kumar et al. (2024), respectively.

Among the evaluated DEMs, Copernicus DEM and NASADEM exhibited the smoothest spectral profiles with minimal high-frequency artifacts, while optical DEMs, particularly ALOS World 3D, showed broad spectral contamination that would compromise the detection of geomorphic changes at hillslope scales.

4.2. Selection of NASADEM as Optimal DEM for Sediment Volume Analysis

Based on the three primary analyses, that is, spectral analysis, void-filled assessment, and spatial analysis of stable areas, NASADEM emerged as the most suitable global DEM for sediment volume calculations in the study area. In stable regions, where no significant topographic changes occurred over time, NASADEM exhibited one of the lowest median errors and standard deviations compared to the LiDAR reference DEM, unlike optical DEMs such as ASTER GDEM, which exhibited high variability across all metrics (Figure 5) due to inconsistencies introduced by variations in atmospheric conditions, sensor calibration, and processing methods over its long acquisition period (Arefi & Reinartz, 2011), or TanDEM-X EDEM, which had higher mean, median, and LE90 values that could potentially overestimate elevations, NASADEM maintained a more balanced elevation representation.

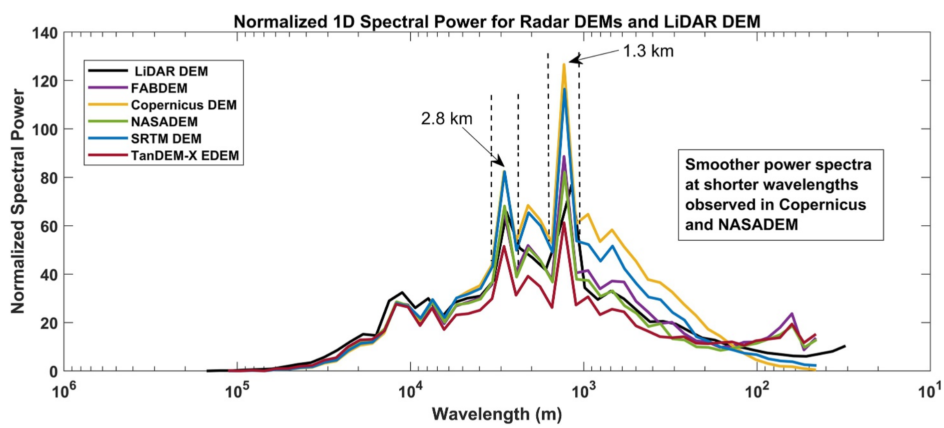

Figure 8. Normalized one-dimensional power spectra envelopes for various radar-based digital elevation models (DEMs) evaluated in this study. Similar dominant wavelengths were observed in both optical and radar-based data sets; however, radar-based DEMs generally exhibit smoother spectra and fewer high-frequency artifacts. Notably, the Copernicus and NASADEM display exceptionally smooth spectral curves with no significant high-frequency peaks, highlighting the enhanced reliability of radar DEMs over their optical counterparts.

While FABDEM and Copernicus DEM performed well in some stable areas, they exhibited higher regional variability due to their void-filling dependencies (Figure 6d).

The void-filled assessment reinforced NASADEM's reliability. Many global DEMs suffer from inconsistencies due to void-filling procedures, where missing data are interpolated or replaced using external data sets of varying resolution and acquisition times. This issue is particularly evident in Copernicus DEM and TanDEM-X EDEM, where voids were predominantly filled using older data sets such as ASTER GDEM, ALOS World 3D, or SRTM, leading to elevation inconsistencies. By contrast, NASADEM was developed as an enhanced version of SRTM, incorporating improved algorithms and additional data sources while maintaining internal consistency. The fact that NASADEM remains largely self-contained with fewer dependencies on external DEMs for void-filling makes it a more suitable choice for sediment volume analysis, as it minimizes potential biases introduced by mixed-source elevation corrections (Figure 6c).

Unlike ASTER GDEM and ALOS World 3D, which exhibited significant noise at small spatial scales, NASADEM maintained a smooth spectral profile comparable to TanDEM-X but without excessive localized distortions (Figure 8). The reduced noise levels in NASADEM ensure that sediment volume estimates are not artificially influenced by spurious short-wavelength artifacts, which can distort elevation differences over time.

Another key factor for selecting NASADEM was the temporal gap between the available global DEM and the 2020 LiDAR DEM. NASADEM provides an extended time interval of nearly two decades, ensuring the accumulation of measurable geomorphological signals resulting from extreme events, such as erosion, sedimentation, and landslide-driven changes, thereby surpassing the detection limits associated with DEM uncertainties (Wheaton et al., 2010). Shorter intervals between surveys often fail to detect significant geomorphic changes or underestimate sediment flux as the time period is insufficient to capture the full range of erosion processes operating at different rates (Daley et al., 2024; Fryirs et al., 2012). Thus, longer intervals, as provided by NASADEM, are essential to reliably capture meaningful geomorphic changes (Daley et al., 2024; James et al., 2012). Given these results, NASADEM was selected as the preferred DEM for sediment volume calculations because of its low spectral noise, minimal void-filling distortions, high vertical accuracy in stable terrain, and appropriate temporal spacing. These characteristics ensure that elevation differences computed from NASADEM reflect true geomorphic changes rather than sensor-induced artifacts or inconsistencies in DEM construction.

4.3. Sediment Volume and Uncertainty Analysis Using NASADEM

The sediment volume and denudation rate analysis revealed substantial sediment fluxes, with thresholded gross erosion of 854.09 Mm^3 and gross deposition of 748.53 Mm^3. The unthresholded net exported volume is 139 ± 44 Mm^3, corresponding to a basin-wide denudation rate of 5.06 ± 1.60 mm/yr. Uncertainty in total sediment volume estimates can arise from a range of factors, including limitations of the instruments used to acquire DEMs, co-registration errors, and systematic or random noise (e.g., sensor drift). The effectiveness of vegetation and vertical bias correction used in our study for reducing uncertainty was demonstrated (Figure 9), with substantial improvements shown by reduced error metrics in stable areas. Without these corrections, the error magnitude would exceed the geomorphic signal in many areas. Vegetation biases alone can exceed 30 m in densely forested regions (Figure S3e in Supporting Information S1), comparable to or exceeding the erosion/depositional signals in many areas, making correction fundamental for change detection. Table 2 highlights the significant reduction in uncertainty after applying vegetation and vertical bias correction. The corrected DoD results in lower random error (σ_{rms}), spatially correlated error (σ_{sc}), and systematic error (σ_{sys}).

For quantifying uncertainty related to vegetation bias correction, we identified pixels requiring vegetation correction, yielding a volumetric uncertainty of 42.41 Mm^3 (Table 3). This vegetation coefficient uncertainty represents the dominant component of the total volumetric uncertainty (43.95 Mm^3), reflecting the inherent challenge of correcting radar-derived elevations for forest canopy effects.

4.4. Spatial Patterns of Erosion and Deposition

The corrected DoD map reveals sediment routing and storage patterns across the Laonong River Basin (Figure 10). Erosional hotspots concentrate in upstream and midstream mountainous regions, where steep slopes and frequent landslides, both riverbank failures and hillslope landslides from tributaries, drive substantial sediment removal. A notable riverbank landslide near the Baolai region (Figure 10c) exemplifies lateral erosion

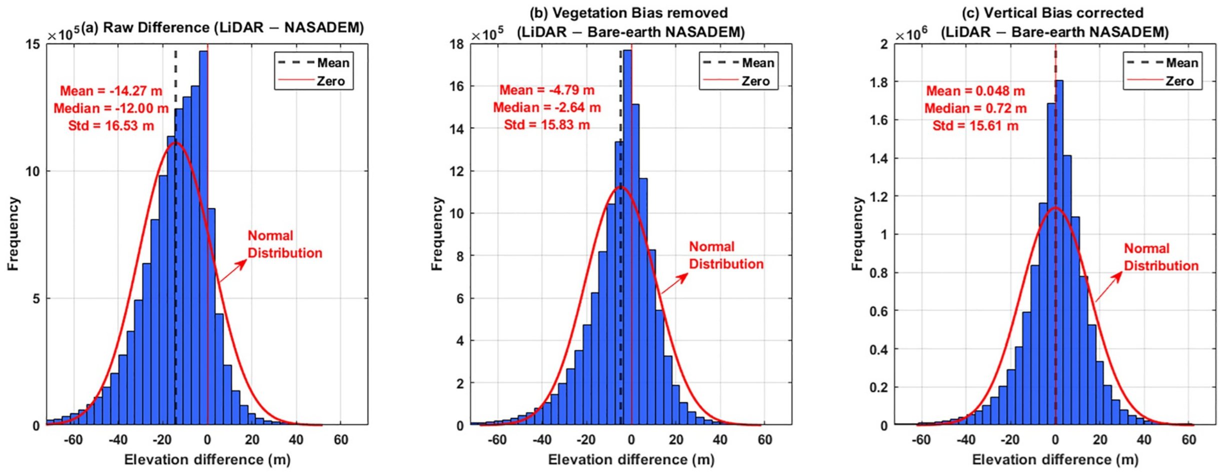

Figure 9. Histograms of the DEMs of difference (DoD) raster for NASADEM before and after corrections. (a) Original DoD relative to the airborne LiDAR reference. (b) After vegetation-bias correction of NASADEM. (c) After residual vertical-bias referencing to LiDAR. The progressive shift of the peak toward zero and the reduced spread indicate the removal of mean vertical bias and decreased variability.

contributing to trunk channel sediment flux. Midstream reaches show extensive aggradation from tributary sediment influx. Among the most significant features influencing sediment redistribution is the Putanpunas landslide (Figure 11), a catchment-scale (~6 km^2) feature within the Laonong River system. Its debris formed a 55 m thick alluvial fan at the tributary junction (Figure 11d), visible as a depositional hotspot in the DoD map.

Analysis of 34 tributary sub-catchments within the Laonong Basin reveals pronounced spatial heterogeneity in decadal erosion rates (Figure 12d; Table S1 in Supporting Information S1). Sub-catchment erosion rates range over three orders of magnitude, from net aggradation (+0.81 mm/yr in sub-catchment 8) to extreme erosion (−550.92 mm/yr in sub-catchment 12, Putanpunas). The sub-catchment mean erosion rate (−15.3 mm/yr, excluding the Putanpunas outlier) and median (−11.4 mm/yr) both exceed the basin-wide average of −5.06 mm/yr by factors of approximately three and two, respectively. Of the 34 sub-catchments, 25 (74%) exhibit erosion rates exceeding the basin average, 6 (18%) show rates at or below the basin average, and 3 (9%, sub-catchments 8, 29, and 32) display net deposition.

The 34 sub-catchments collectively occupy 1,161 km^2 and produce a net sediment export of −367.32 Mm^3 over the 20-year study period. The midstream sub-catchments between Baolai and Taoyuan (11–17) concentrate one of the highest erosion rates within the Laonong River, with six sub-catchments exceeding 15 mm/yr. The downstream sub-catchments (particularly western sub-catchments 26, 29, and 32) exhibit low to moderate sediment erosion, contributing relatively less to the main channel's aggradation.

Table 3
Parameters Used to Estimate Volumetric Uncertainty Associated With Vegetation Bias Correction

n_{veg}	84,155 pixels
Mean CHM	17.30 m
Mean ρ	0.73
Mean(CHM × ρ)	17.30 × 0.73 = 12.63 m
Δa	0.1
σ_{VB}	0.1 × 12.63 = 1.26 m
$\sigma_{v,\mathrm{veg}}$	42.41 Mm^3

Note. Vegetated pixels in 2,000 were identified using the Hansen Global Forest Change tree cover data set, with a fractional tree cover threshold of 0.25 (Hansen et al., 2013; Tyukavina et al., 2015). The vegetation coefficient uncertainty ($\Delta a = 0.1$) reflects the established range (0.5–0.6) of empirically derived scaling coefficients for C-band radar vegetation correction (Carabajal & Harding, 2005; O'Loughlin et al., 2016).

To quantify sediment storage partitioning, the DoD was classified into three process zones. Zone 1 comprises the tributary sub-catchments excluding valley floor deposits. Zone 2 encompasses valley floor deposits, subdivided into deposits within sub-catchment boundaries (Zone 2a) and main channel corridor deposits (Zone 2b), and Zone 3 represents residual interstitial areas outside Zones 1 and 2. The zone-partitioned sediment budget (Table S2 in Supporting Information S1) shows that of the 854.09 Mm^3 of thresholded basin-wide gross erosion, 194.61 Mm^3 was re-deposited locally on hillslopes and in small channels (Zone 1), 525.57 Mm^3 was captured by valley floor deposits (Zone 2), and 28.35 Mm^3 accumulated in residual interstitial areas (Zone 3), yielding a basin-wide storage total of 748.53 Mm^3.

4.5. Longitudinal Cumulative Sediment Flux Profile

To examine the spatial organization of sediment production and storage along the Laonong River system, we computed cumulative erosion, deposition, and

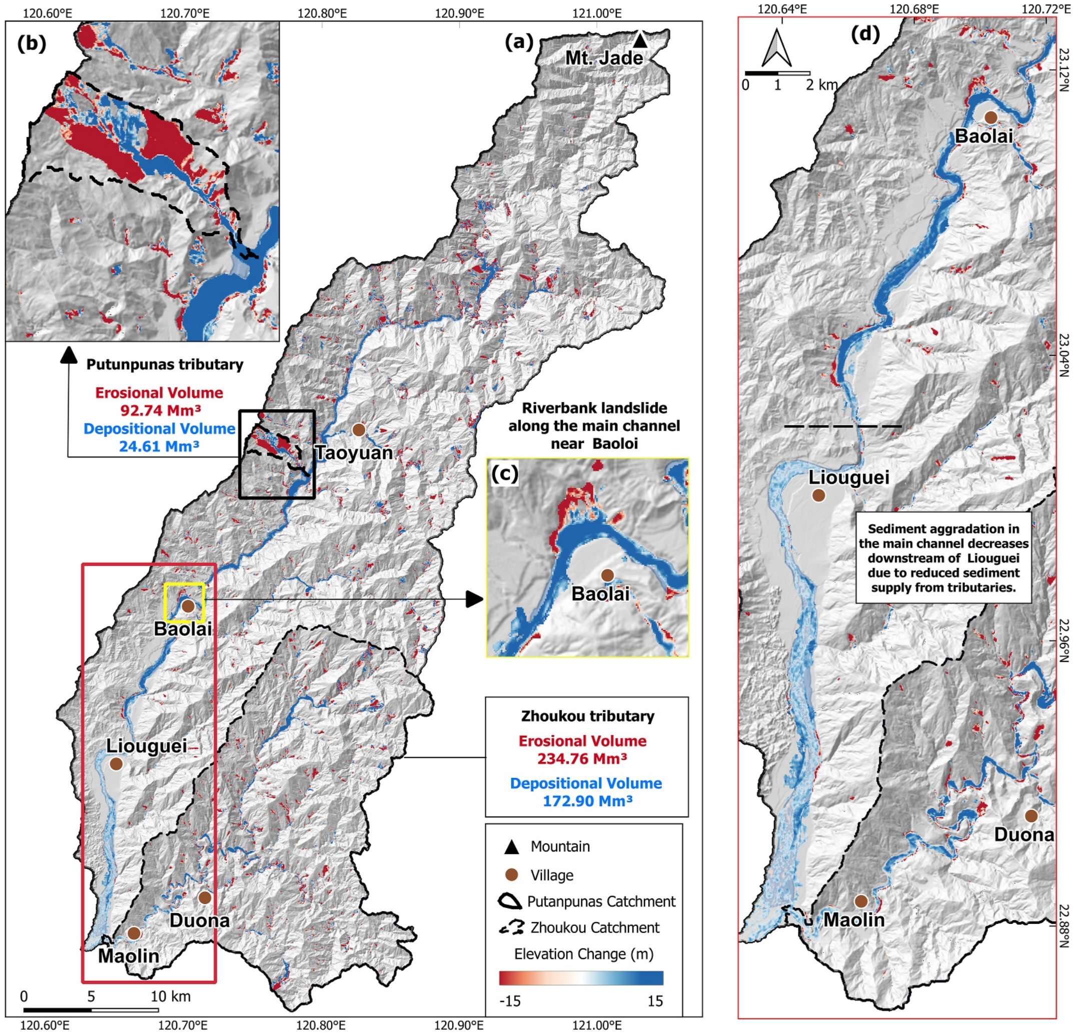

Figure 10. (a) DEMs of difference Map of the Laonong River Basin for the period 2000–2020 illustrating the elevation difference map for the entire basin, showing sediment deposition (blue) in landslide toes and river channels, and sediment erosion (red) in landslide scars and along eroding riverbanks. (b) Putanpunas tributary, the largest landslide complex in the catchment, showing erosional volume (92.74 Mm^3) and depositional volume (24.61 Mm^3). (c) Riverbank landslide near Baolai illustrating lateral erosion and associated channel deposition. (d) Main channel corridor from Baolai to Maolin showing aggradation intensity decreasing downstream of Liouguei.

net sediment export as functions of downstream distance along the main channel (Figure 13). This analysis encompasses 998 km^2 of the basin before the Zhoukou tributary joins the main stream.

The longitudinal profile reveals a systematic downstream increase in cumulative erosion, reaching approximately 620 Mm^3 before joining the Zhoukou Tributary (Figure 13a). Cumulative deposition follows a strikingly parallel trajectory, attaining 575 Mm^3 over the same distance. The close correspondence between these curves with deposition consistently tracking cumulative erosion in the lower basin provides direct evidence for efficient sediment buffering within the basin. Net sediment export totals approximately 51 Mm^3 (unthresholded), confirming that the vast majority of eroded material is stored within the basin.

The cumulative denudation rate (Figure 13b) exhibits pronounced spatial structure. Headwater reaches (0–20 km) show relatively modest rates of 2–4 mm/yr, reflecting the predominance of persistently forested terrain with limited landslide activity. Between 20 and 35 km, rates increase sharply to a maximum of 12.9 mm/yr, coinciding with the entry of several high-yield tributary systems, including sub-catchment 1 (177 km^2, 6.6 mm/yr) and sub-catchment 5 (105 km^2, 20.5 mm/yr). The mid-basin zone (35–60 km) sustains elevated rates of 8–11 mm/yr,

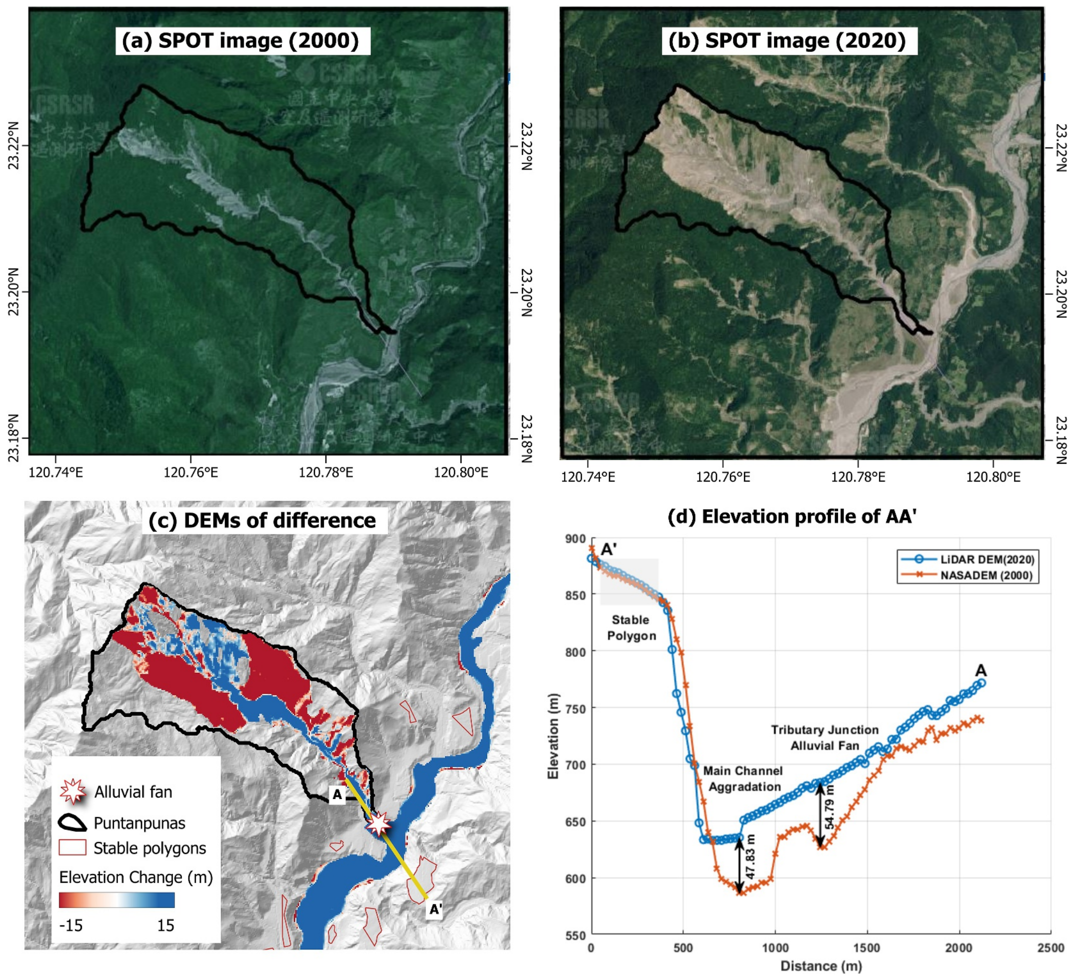

Figure 11. Top panel (a–b): Satellite images of Putanpunas catchment 20 years apart. An extreme event such as Typhoon Morakot significantly altered the topography, and its impact remains evident in the catchment. The bottom-left panel (c) illustrates elevation changes over the past two decades, highlighting massive aggradation in the main channel of the Laonong River due to a deep-seated landslide. Additionally, the formation of a debris fan at the tributary-main channel junction is notable, with elevation changes reaching nearly 55 m. The aggraded main channel and the debris fan at the tributary-main channel junction acted as primary sediment buffer zones within the basin, delaying downstream sediment evacuation, as evident from the DEMs of difference map. The bottom-right panel (d) presents the elevation profile of cross-section AA', clearly showing the main channel aggradation and debris fan accumulation. Notably, the profile line also passes through one of the stable polygons, which has been used for spatial stable area analysis. This stable polygon, located on a high flat terrace away from landslides and active channels, has remained relatively stable over the past two decades with no significant geomorphological changes. *Credit: satellite images, SPOT © CSRSR, NCU, Taiwan.*

encompassing the confluence of sub-catchments characterized by active mass wasting, including the Putanpunas landslide complex (sub-catchment 12; 6.5 km^2, 550.92 mm/yr).

A distinctive inflection occurs near 59 km, where a single step contributes 116 Mm^3 of cumulative erosion, the largest discrete sediment input along the profile. This zone corresponds to the Putanpunas tributary junction, where catastrophic landsliding during Typhoon Morakot generated massive debris flows that deposited the thick alluvial fan at the confluence with the trunk channel (Figure 11). The concurrent increase in cumulative deposition demonstrates that substantial proportions of this sediment pulse were immediately sequestered within the valley fill rather than exported downstream.

Downstream of the Putanpunas zone (>75 km), cumulative denudation rates decline progressively from 7 mm/yr to 2.6 mm/yr at the profile terminus. This attenuation reflects both the incorporation of lower-yield tributary catchments and the dominance of depositional processes in the widening valley floor.

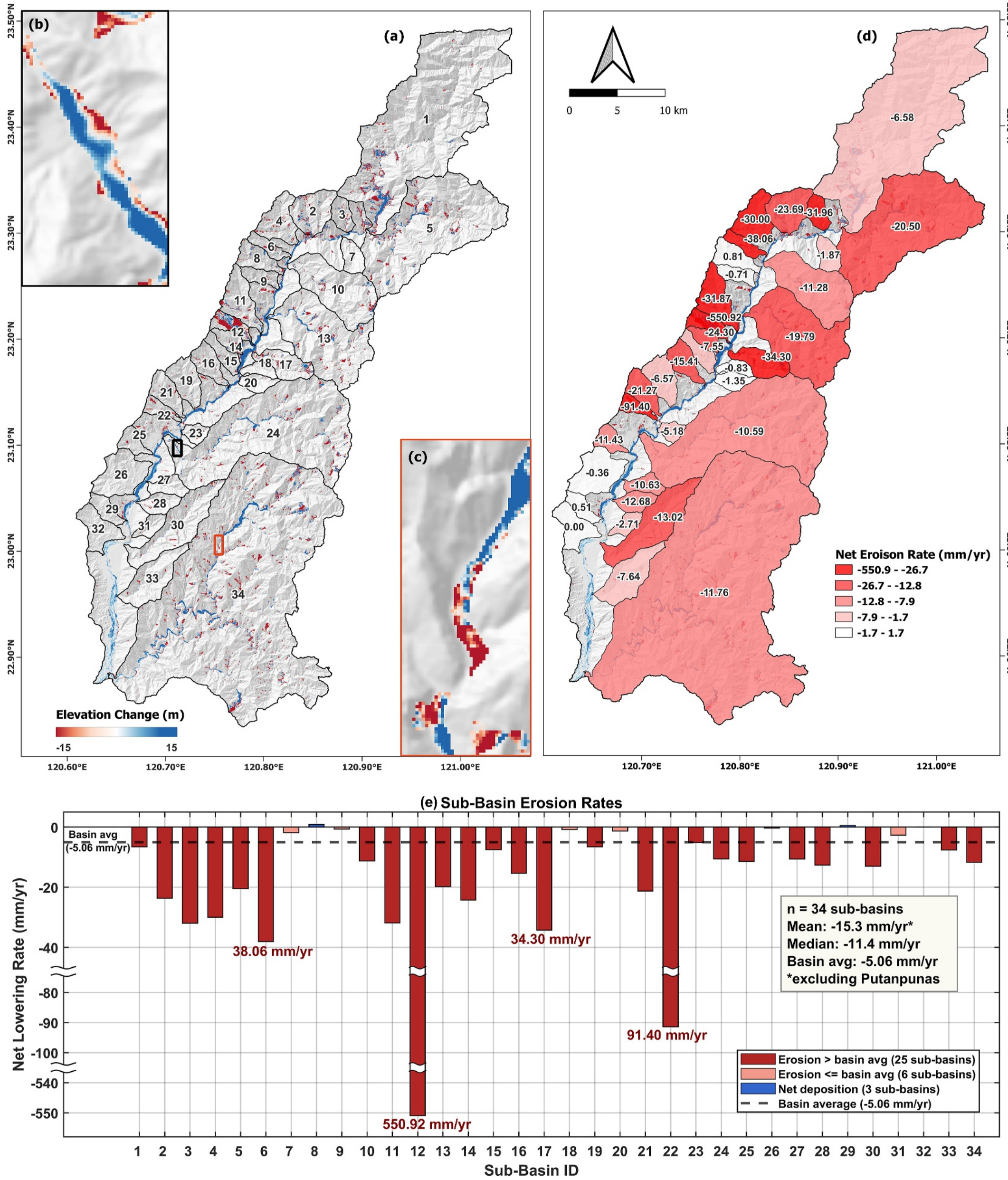

Figure 12. Sub-catchment erosion rate variability in the Laonong River Basin. (a) Index map overlaid on DEMs of difference map with 34 numbered tributary sub-catchments showing erosion (red) and deposition (blue). Insets show (b) lateral channel erosion example and (c) segment of tributary channel showing incision (d) Sub-catchment erosion rates (mm/yr) by category; note extreme value in sub-catchment 12 (Putanpunas, −550.9 mm/yr). (e) Erosion rates for all sub-catchments; dashed line indicates basin-wide average (−5.06 mm/yr).

4.6. Erosion Rates Derived From Gauge-Station Based Rating Curve Method

Suspended-sediment derived erosion rates estimated using the gauge-station based rating curve method are consistently lower than erosion rates derived from DoD for the common study period (2000–2020). Rating-curve based erosion rates were calculated at three hydrological stations within the Laonong River Basin and ranged from 0.57 to 4.39 mm yr^{-1} over the study interval (Table 4).

The lowest erosion rates were obtained at stations representing longer multi-year records, whereas the highest value corresponds to a short observation window dominated by elevated discharge conditions. Station coverage within the basin reflects changes in monitoring infrastructure following major extreme events. The original outlet

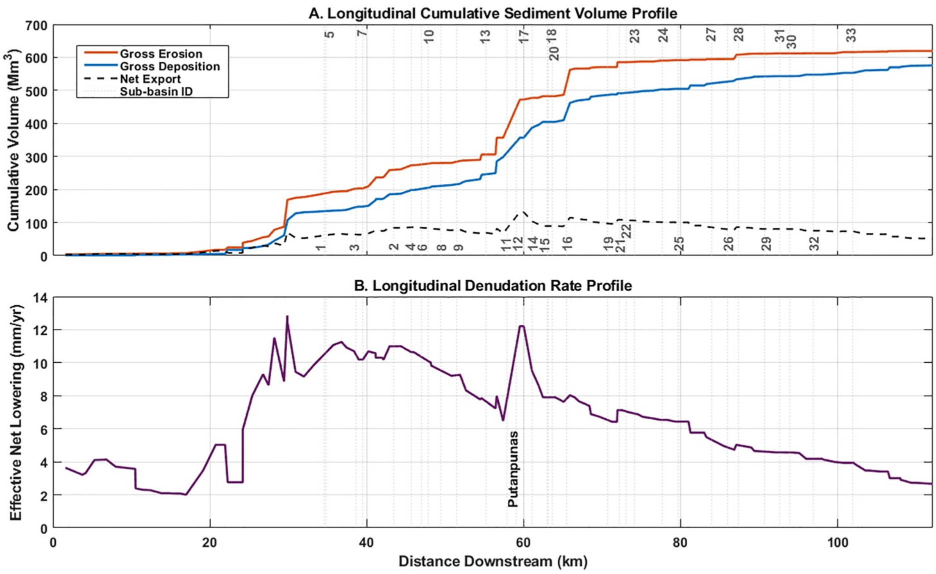

Figure 13. Longitudinal cumulative sediment flux profile along the Laonong River main channel (2000–2020) computed upstream of the Zhoukou tributary confluence and encompassing approximately 998 km^2 of the 1,373 km^2 basin. (a) Cumulative gross erosion (red), gross deposition (blue), and net export (dashed black) volumes as functions of downstream distance. Vertical dashed lines mark the confluences of tributary sub-catchments, labeled by the ID number. Gross erosion and deposition are thresholded (LoD = ±1.82 m; Anderson, 2019); net export is unthresholded and therefore does not equal the arithmetic difference between the two gross curves. The close parallelism between gross erosion and deposition curves demonstrates pervasive sediment buffering, with deposition consistently tracking erosion throughout the lower basin. (b) Cumulative basin-averaged denudation rate showing peak values of 10–13 mm/yr in the mid-basin zone (35–60 km), declining to approximately 2.5 mm/yr at the downstream end of the profile. The rate decline reflects progressive sediment storage along the channel network rather than diminishing erosion intensity.

gauge station (1730H039) was destroyed during the 2009 Typhoon Morakot, temporarily replaced by an upstream station (1730H060), and subsequently re-established at the same location as station 1730H070, resulting in temporally segmented sediment and discharge records.

Daily water discharge records were used to reconstruct suspended sediment fluxes via station-specific rating curves (Figure 14). The rating curve exponent decreased from 1.54–1.63 (before and immediately after Typhoon Morakot) to 1.09 (during the recovery period), while the coefficient increased from 3.9 to 29. The elevated coefficient reflects greater sediment availability at all discharges, while the near-unity exponent indicates that suspended sediment concentrations increase roughly proportionally with discharge, a signature of transport-limited conditions where abundant channel-stored sediment from Morakot-triggered landslides is readily entrained even during moderate flows. This contrasts with the pre-Morakot regime ($b > 1.5$), when sediment concentrations increased nonlinearly with discharge, requiring higher flows to access additional sediment sources. All three periods show strong Q_s–Q correlations ($R^2 = 0.76$–0.86). However, substantial temporal gaps

Table 4
Suspended-Sediment Derived Erosion Rates From Rating-Curve Analysis (2000–2020)

Gauge station number	Drainage area (km^2)	Years in record	Number of sediment observations	Mean water discharge (CMS)	Mean sediment concentration (ppm)	Mean suspended load (10^3 kg/day)	Sediment transport rate (Mm^3/yr)	Erosion rate (mm/yr)
H039	885	2000–2009	311	57.4	813.7	4,035.66	0.53	0.59
H060	870	2010	30	69.5	4,531.8	27,223.2	3.82	4.39
H070	885	2011–2020	299	85.4	546.8	4,033.2	0.50	0.57

Note. Suspended sediment loads were reconstructed using station-specific rating curves (Q_s = AQ^B) applied to available daily discharge records. The number of sediment observations reflects spot measurements available within the period reported for each gauge station. Sediment transport rate is converted assuming a bulk rock density of 2.6×10^3 kg m^{-3} (Fuller et al., 2003).

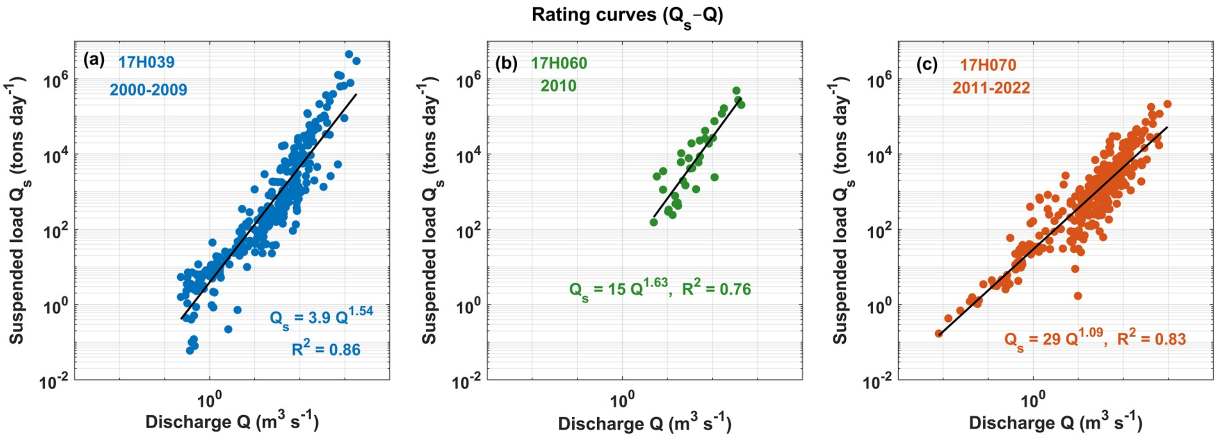

Figure 14. Suspended sediment load (Q_s) versus water discharge (Q) rating curves for Laonong River gauge stations: (a) H039, pre-Morakot (2000–2009) (b) H060, immediate post-Morakot (2010) and (c) H070, post-Morakot recovery (2011–2022). The rating curve exponent decreased from 1.54–1.63 (before and immediately after Typhoon Morakot) to 1.09 (during the recovery period), while the coefficient increased from 3.9 to 29. All three periods show strong Q_s–Q correlations ($R^2 = 0.76$–0.86) within the sampled discharge range.

are present in the discharge time series (Figure 3a), particularly during periods immediately before and after extreme rainfall events. These gaps coincide with intervals when high-magnitude floods are most likely to occur, indicating that some extreme flow conditions were not captured in the gauge records. Because extreme events in Taiwan's mountain rivers can account for more than ~75% of total sediment export (Kao et al., 2005), missing high-flow data introduce uncertainty and likely lead to an underestimation of suspended-sediment derived erosion rates.

5. Discussion

5.1. Sediment Storage and Buffering: Evidence From DoD Analysis

The spatial patterns documented in Sections 4.4–4.5 provide clear evidence for a significant sediment buffering effect within the Laonong River Basin. Despite tributary erosion rates ranging from 2 to 100 times the basin average, 87.6% of thresholded gross erosion was stored within the basin (Table S2 in Supporting Information S1), partitioned among local hillslope re-deposition (22.8%), major valley floor deposits (61.5%), and residual interstitial areas (3.3%). This internal sediment sequestration, manifesting as tributary alluvial fans, landslide deposits, valley fills, and sediment blankets in the trunk channel, acts as a buffering mechanism, dampening the expression of high local erosion rates at the catchment outlet. This behavior aligns with studies reporting that sediment delivery ratios tend to decrease with increasing catchment area due to internal storage (Dedkov, 2004; Walling, 1983).

The parallelism between cumulative erosion and deposition curves (Figure 13) demonstrates that buffering operates as a distributed process along the entire fluvial network and is not confined to isolated depositional nodes. At each downstream increment, newly eroded sediment is substantially offset by concurrent deposition, maintaining a relatively constant net export flux despite large variations in local erosion intensity. The downstream attenuation of cumulative denudation rates, from peak values of 12.9 mm/yr in the mid-basin to 2.7 mm/yr upstream of the Zhoukou confluence, reflects the cumulative integration of both erosional sources and depositional sinks along the channel network.

Research on large continental basins (area $\gtrsim 10^5$–10^6 km^2) such as the Amazon (Wittmann et al., 2011), Indus (Clift & Giosan, 2014), and global-scale analyses (Ben-Israel et al., 2022; Covault et al., 2013) demonstrates that sediment residence times can span thousands to millions of years, muting and delaying sediment flux out of the basin. Our results demonstrating the observed difference between high local erosion rates and lower outlet sediment flux in the Laonong Basin reinforces the idea that buffering can be substantial even in relatively small meso-basin scales of the Laonong (1,373 km^2), high-relief catchments, filtering erosional signals and controlling sediment delivery over decadal timescales.

The DoD reveals substantial net aggradation across the basin, with up to 48 m of deposition in the main trunk channel at major tributary junctions (Figure 11d). The sediment retention documented in valley floor deposits (Table S2 in Supporting Information S1; 61.5% of gross erosion) indicates that the basin remained in a storage-dominated phase throughout the 2000–2020 study period. These patterns parallel post-cyclone responses documented in New Zealand, where tributary-junction fans act as temporary sediment buffers with aggradation reaching tens of meters (Leenman & Tunnicliffe, 2019; Tunnicliffe et al., 2018). The overall positive sediment budget (erosional volume exceeding exported volume) reflects incomplete evacuation of sediment mobilized during extreme events within the study period.

Several factors contribute to this prolonged storage phase. Continued hillslope supply from active features such as the Putanpunas landslide maintains sediment input (Tseng et al., 2019), while insufficient flood magnitudes have failed to mobilize thick sediment armor layers (Kumar et al., 2024; Sklar & Dietrich, 2004). The DoD map reveals thick, coarse sediment layers blanketing midstream riverbeds, which would inhibit bedrock incision under typical flow conditions. While localized incision occurs in some tributary segments (Figure 12c), the majority of the main channel remains in a non-incising state, consistent with decadal-scale sediment persistence following major disturbances (DeLisle et al., 2022; Ruetenik et al., 2024). The watershed's landslide ratio has not yet returned to pre-Morakot levels (Tseng et al., 2020), indicating incomplete geomorphic recovery more than a decade after the event.

Critically, sediment evacuation from mountain river systems is fundamentally event-driven. Coarse channel fill and fan deposits require threshold-exceeding floods for remobilization (Hassan et al., 2005; Lisle et al., 2001). The 2011–2020 period was hydrologically quiescent relative to preceding decades, with no events approaching Morakot's magnitude (Kumar et al., 2024). Without such threshold-exceeding floods, substantial valley storage persists regardless of the elapsed time since the initial disturbance. This interpretation aligns with global observations that coarse sediment pulses from extreme events persist for decades to centuries awaiting evacuation. In California's Sierra Nevada, hydraulic mining sediment (1853–1884) continues to be reworked more than 100 years later (James, 1999; Singer et al., 2013), while in New Zealand, sediments deposited by the 1988 Cyclone Bola remain identifiable in the Waipaoa River system after more than three decades (Tunnicliffe et al., 2018). At the global scale, coarse sediment residence times in mountain basins range from 10^2 to 10^4 years depending on storage dynamics and disturbance frequency (Carretier et al., 2020; Hoffmann, 2015). The 87.6% storage efficiency observed in the Laonong Basin is consistent with these global patterns, representing early-stage sequestration of a sediment pulse that may require decades to centuries for complete evacuation.

While quantifying evacuation timescales as a function of future event frequency and magnitude requires further research, the current distribution of stored sediment has immediate implications for hazard assessment. Prolonged sediment storage could set the stage for devastating impacts similar to Nepal's Melamchi Valley during the 2021 flood, where remobilization of stored sediment caused severe downstream damage (Chen et al., 2025). The longitudinal profile identifies specific zones of heightened remobilization potential. The 48-m aggradational package adjacent to the Putanpunas confluence represents approximately 49 Mm^3 of readily mobilizable sediment, while distributed valley-fill deposits between 40 and 80 km constitute a continuous sediment reservoir whose stability depends on maintenance of channel armor layers. The DoD-derived spatial mapping of these storage zones provides essential baseline data for forecasting the potential impacts of future extreme events on downstream infrastructure.

5.2. Comparison of Erosion Rates Across Spatial and Temporal Scales in the Basin

Erosion rates derived from the Laonong River Basin (~5 mm/yr) contrast markedly with rates observed in smaller tributaries, which extend up to 550 mm/yr. This difference reflects how erosion rates from larger basins incorporate a wider array of geomorphic processes, averaging localized high-intensity erosion episodes over broader spatial scales. In contrast, smaller tributary catchments are particularly sensitive to episodic catastrophic events such as landslides triggered by extreme precipitation or seismic activity, temporarily inflating their apparent sediment yields (Dadson et al., 2003, 2004). Sub-catchment analysis reveals that 74% of tributary catchments erode faster than the basin-wide average, with mean sub-catchment erosion rates (15.3 mm/yr) approximately three times higher than the integrated basin rate (5.06 mm/yr).

The extreme rate in Putanpunas (550.92 mm/yr) highlights the heavy-tailed distribution characteristic of landslide-dominated sediment production (Hovius et al., 1997; Stark & Guzzetti, 2009). This sub-catchment represents the legacy of the 2009 Typhoon Morakot, which triggered a catastrophic deep-seated landslide eroding ~93 Mm^3 of material. Despite comprising only 0.5% of the total basin area, Putanpunas accounts for approximately 12% of the total sub-catchment erosion volume, demonstrating how episodic mass-wasting events dominate decadal sediment budgets in tectonically active orogens. Similarly, the Zhoukou tributary (sub-catchments 34, 11.76 mm/yr) erodes at approximately twice the basin-wide average despite its large area (374 km^2), consistent with DoD analysis documenting widespread hillslope erosion throughout this tributary system (Kumar et al., 2024).

The divergence between sub-catchment and basin-wide erosion rates highlights the limitations of conventional monitoring approaches. Gauge station sediment flux data, typically limited to catchment outlets, integrate all upstream inputs and inherently capture a buffered signal rather than the hillslope source signal. These estimates are also subject to systematic biases. Basin gauge stations averaged only ~30 sediment concentration measurements per year during 2000–2020 (Figure 3b), requiring rating curve extrapolation across the majority of the hydrographs. Moreover, instrumentation failure during extreme events creates critical data gaps precisely when sediment flux and water discharge are at their peaks. The WRA record contains no measurements during Typhoon Morakot (Figure 3), likely resulting in substantial underestimation of decadal sediment export (Kao et al., 2005; Kao & Milliman, 2008).

DoD analysis overcomes these limitations by resolving internal spatial heterogeneity and identifying concentrated geohazard zones invisible in outlet-integrated measurements. Sub-catchments 6, 12, 17, and 22, for example, erode at rates 7–110 times the basin average. However, the main channel corridor intercepts the majority of this material, functioning as a capacitor that smooths erosional signals across space and explains the coexistence of localized extreme erosion with moderate basin-outlet sediment flux.

To enable direct comparison with Dadson et al. (2003), we calculated a DoD-derived lowering rate for the area draining to the gauge location (~812 km^2, station 1730H031), yielding ~5.03 mm/yr. This is consistent with their suspended sediment-derived estimate of 6.4 ± 1.5 mm/yr for 1970–1999 at the same location. These two estimates are derived from fundamentally different measurement approaches, volumetric elevation change versus suspended sediment flux and cover different time periods, yet fall within each other's uncertainty envelopes. This convergence is particularly significant because the 2000–2020 period encompasses the 2009 Typhoon Morakot, which triggered widespread catastrophic landsliding and debris flows that mobilized substantial volumes of sediment across the basin. Despite this, the basin-scale DoD rate does not exceed the pre-Morakot (1970–1999) suspended sediment estimate, consistent with the sediment buffering documented in Section 5.1. By contrast, gauge-derived rates for 2000–2020 (0.57–4.39 mm/yr) are lower, illustrating the systematic underestimation that results when monitoring records are truncated by the very events that dominate sediment transport. Beyond the decadal timescale, the basin-wide DoD rate of 5.06 ± 1.60 mm/yr aligns with independent estimates across multiple temporal scales (Table 5): cosmogenic nuclide-derived (^{10}Be) denudation rates of ~2.5 ± 0.5 mm/yr for the Laonong River (Derrieux et al., 2014), magnitude-frequency based estimates of ~2.7–5.2 mm/yr for the broader Kaoping watershed over 1957–2009 (Chen et al., 2014), and the general understanding that erosion rates within Taiwan's mountain belts typically range between 3 and 6 mm/yr across all timescales (Dadson et al., 2003). The consistency between our decadal volumetric measurement and these millennial-to-million-year estimates suggests that, when integrated over sufficient catchment area, the Laonong Basin operates near a long-term erosional steady state in which extreme events, though locally devastating, are absorbed into a rate that remains broadly stable across measurement timescales.

This apparent temporal consistency of erosion rates in the Laonong River Basin is consistent with the time-scale invariance of denudation rates documented by Sadler and Jerolmack (2015). Their global compilation demonstrates that upland denudation rates, when determined from specific sediment yield integrated over whole catchments, show little or no dependence on measurement intervals from annual to million-year timescales. This time-invariance emerges because spatial averaging across catchment areas captures active and inactive erosional patches in representative proportions, eliminating the noise introduced by intermittent processes such as landsliding (Sadler & Jerolmack, 2015). Our basin-wide DoD-derived rate represents precisely this kind of spatially integrated measurement, which explains its alignment with longer-term estimates despite capturing extreme events such as Typhoon Morakot (Figure 3). Recent work by Halsted et al. (2025) supports this mechanism, documenting widespread sediment storage and burial signatures in basins >1,000 km^2 globally. Thus, apparent steady-state conditions in the Laonong Basin represent "pseudo-equilibrium" where buffering masks true landscape transience.

10.1029/2025JF008720

Table 5
Estimates of Erosion Rates Across Multiple Timescales for the Laonong River Basin

Basin/Region	Method/Proxy	Time period	Rate (mm/yr)	Source	Notes
Laonong River Basin	DEM differencing	2000–2020	5.06 ± 1.60	This study	Basin-integrated modern export during climate extremes
Zhoukou River (tributary)	DEM differencing	1990–2020	10–14	Kumar et al. (2024)	Small basin; limited sediment buffering
Kaoping watershed	Magnitude–frequency/event integration	1957–2009	2.7–5.2	Chen et al. (2014)	Regional event-driven export
Laonong (Gauge station, 1730H031)	Suspended sediment load → erosion rate	1970–1999	6.4 ± 1.5	Dadson et al. (2003)	Station drainage ~812 km^2; does not cover full Laonong basin (1,373 km^2)
Laonong River Basin	^{10}Be cosmogenic nuclides	Millennial	2.5 ± 0.5	Derrieux et al. (2014)	Long-term denudation
Taiwan mountain belt	Modern river sediment loads + Holocene bedrock strath incision + thermochronometry	10^1–10^6 yr	3–6	Dadson et al. (2003)	Taiwan-scale synthesis
Central Range (Taiwan)	Fission-track thermochronology + modeling	Myr	~2.3–3.3	Fuller et al. (2006)	Long-term exhumation

While erosion measurements from large basins are significant for interpreting mountain-building processes and landscape evolution, exclusive reliance on outlet-integrated data overlooks critical localized hazard potentials. Smaller tributary catchments generate high sediment fluxes with severe downstream consequences including floods and extensive channel aggradation. In the Laonong Basin, aggradation patterns identified through DoD analysis indicate potential for future slope instability, as demonstrated in the nearby Xinwulü River where cyclical erosion and aggradation destabilized slopes (Lo et al., 2021). Severe sedimentation in the Laonong River has already triggered major disruptions, including suspension of the Tseng-Wen Reservoir Transbasin Diversion Project (Hsieh & Capart, 2013). DoD analyses thus provide essential spatial distribution for identifying sediment source areas and prioritizing hazard mitigation, information unavailable from conventional gauging approaches that capture only sediment outflux at catchment outlets.

5.3. Limitations and Future Directions

Pixels with persistent vegetation cover in both the DEMs, where reliable elevation change cannot be resolved, were masked out and excluded from both the volume calculation and uncertainty analysis. We assume a negligible net change in these masked areas. However, this exclusion may result in an underestimation of the true basin-wide uncertainty.

Another likely limitation in the study relates to water-covered surfaces, which may introduce localized uncertainties. However, these active water surface features are typically sub-pixel in width (often <1 pixel at the 30 m resolution), making their overall contribution to volumetric estimates negligible at the basin scale. The observations from the ESRI 2020 Land Use/Land Cover (LULC) map at 10-m resolution (Figure S5 in Supporting Information S1) clearly indicate that water pixels only occupy a small fraction of the valley corridor and are spatially discontinuous.

The selection of NASADEM in this study may be limited by site-specific factors such as acquisition timing, limited void filling, and reduced high-frequency noise. Nonetheless, its C-band system, with ∼40–60% canopy penetration, provides a more representative ground approximation than X-band DEMs (Becek, 2008; Kenyi et al., 2009), making it particularly suitable for densely vegetated, high-relief terrain. Importantly, its short acquisition window in February 2000 offers a temporally coherent baseline for change detection, minimizing uncertainties associated with multi-temporal mosaics. Reprocessing improvements, including advanced phase unwrapping and integration of ICESat control points, reduce vertical RMSE relative to SRTM (Crippen et al., 2016), while comparative studies confirm its superior performance in forested mountains globally (Li et al., 2022; Okolie et al., 2024). Remaining limitations stemming from spatial variability in canopy structure and residual vegetation biases could be further constrained by integrating NASADEM with contemporary canopy height models.

For future geomorphic applications, NASADEM provides an increasingly valuable baseline; its discrete 11-day capture in 2000 and growing temporal separation ensure that genuine surface changes progressively exceed measurement noise in active mountain regions. Broader use of NASADEM in tropical and subtropical environments, where dense vegetation and relief limit conventional DEM differencing, could advance long-term sediment budgeting and hazard assessment. Future work could further develop and benchmark frequency-based correction workflows, particularly in geomorphologically dynamic regions where traditional stable-area approaches are constrained. A hybrid framework, combining sparse stable patches with frequency-domain filtering, may ultimately expand the applicability of DEM differencing to regions previously considered challenging for robust change detection.

6. Conclusion

This study demonstrated that decadal erosion rates in Taiwan's Laonong River Basin align with millennial averages, even after decades marked by extreme rainfall events. We attribute this consistency to sediment buffering, which moderates basin-scale erosion signals through internal storage. Our analysis identifies NASADEM as the most suitable global DEM for quantifying geomorphic change, owing to its vertical consistency, minimal void filling, and fewer high-frequency artifacts, making it particularly well-suited for decadal-scale sediment monitoring in mountainous regions. Vegetation and vertical bias corrections further improved DEM differencing, reducing volumetric uncertainty from ∼187 to ∼44 Mm^3 and allowing more reliable estimates of sediment export.

At the basin scale, the estimated erosion rate of 5.06 ± 1.60 mm/yr represents a regionally integrated measure of decadal denudation. In contrast, sub-catchment erosion rates range up to 550.92 mm/yr (Putanpunas), with a mean of 15.30 mm/yr across the remaining tributaries, illustrating the intensity of localized disturbance. These contrasts show why traditional gauging-station networks, typically confined to basin outlets due to economic constraints, may underrepresent erosional variability within mountain basins. The DoD-derived rate is independently corroborated by the suspended sediment-derived estimate of 6.4 ± 1.5 mm/yr reported by Dadson et al. (2003) for 1970–1999 at the common gauge station location, demonstrating convergence across measurement approaches despite encompassing Typhoon Morakot within the DoD measurement period. The patterns observed here point to the importance of internal sediment storage, including hillslope re-deposition, valley-fill deposits, tributary-junction fans, and channel aggradation zones, which collectively retain 87.6% of mobilized sediment within the basin and delay export to the outlet. Evidence of ongoing aggradation and limited incision suggests that the Laonong River remains in a storage phase, with future adjustments dependent on the magnitude of events capable of mobilizing coarse channel deposits. Such episodic aggradation-incision cycles complicate sediment budgets and must be considered when linking short-term changes to long-term landscape evolution. Taken together, these results emphasize the dual importance of sediment storage and scale in shaping erosional signals. The results also highlight the importance of legacy global DEMs such as NASADEM, which, once corrected, remain valuable for reconstructing geomorphic responses to extreme events and enabling sediment budgeting and hazard analysis in data-sparse mountainous terrain.

Conflict of Interest

The authors declare no conflicts of interest relevant to this study.

Availability Statement

NASADEM (NASA JPL, 2020) and SRTM DEM (NASA JPL, 2013) are available from NASA's Earthdata portal (https://earthdata.nasa.gov). The ALOS World 3D (AW3D30) dataset (Japan Aerospace Exploration Agency, 2021) can be accessed through the Japan Aerospace Exploration Agency (https://www.eorc.jaxa.jp/ALOS/en/dataset/aw3d30/aw3d30_e.htm). Copernicus GLO-30 DEM (European Space Agency, 2024) is distributed by the European Space Agency and is available via OpenTopography (https://doi.org/10.5069/G9028PQB). FABDEM (Hawker et al., 2022) is available at (https://data.bris.ac.uk/data/dataset/s5hqmjcdj8yo2ibzi9b4ew3sn). The TanDEM-X 30 m Edited DEM (EDEM) (German Aerospace Center, 2023) can be downloaded from the German Aerospace Center (DLR) portal (https://download.geoservice.dlr.de/TDM30_EDEM/). The ASTER GDEM (LP DAAC, 2019) is distributed by NASA and METI and can be obtained from the Earthdata platform (https://asterweb.jpl.nasa.gov/gdem.asp). The 20 m DEM is provided by the Ministry of Interior, Taiwan. The processed DEM subset used in this study is archived on Zenodo at https://doi.org/10.5281/zenodo.19625289 (Kumar, 2026) to ensure accessibility and reproducibility. MATLAB scripts used for Fourier transformation and spectral analysis of DEMs are available on Zenodo at https://doi.org/10.5281/zenodo.19807252 (Purinton, 2026).

Acknowledgments

This work is supported by the National Science and Technology Council of Taiwan under grant NSTC113-2119-M-259-004 and NSTC113-2116-M-001-018. We acknowledge the support and resources provided by the Taiwan International Graduate Program, the Institute of Earth Sciences, Academia Sinica, Taiwan, and the Department of Earth Sciences, National Central University. The authors would like to thank the Editor, Associate Editor, and all the anonymous reviewers for their constructive comments and suggestions across multiple rounds of revision. We particularly wish to acknowledge one reviewer whose detailed comments and insightful suggestions across all rounds of revision have fundamentally improved this work. We also sincerely thank the Associate Editor's substantive suggestions, which helped in refining the manuscript's clarity and content.

References

Airbus, D. S. (2020). Copernicus DEM: Copernicus digital elevation model validation report. *Airbus Defence and Space-Intelligence*.

Andermann, C., Crave, A., Gloaguen, R., Davy, P., & Bonnet, S. (2012). Connecting source and transport: Suspended sediments in the Nepal Himalayas. *Earth and Planetary Science Letters*, *351–352*, 158–170. https://doi.org/10.1016/j.epsl.2012.06.059

Anderson, S. W. (2019). Uncertainty in quantitative analyses of topographic change: Error propagation and the role of thresholding. *Earth Surface Processes and Landforms*, *44*(5), 1015–1033. https://doi.org/10.1002/esp.4551

Arefi, H., & Reinartz, P. (2011). Accuracy enhancement of ASTER global digital elevation models using ICESat data. *Remote Sensing*, *3*(7), 1323–1343. https://doi.org/10.3390/rs3071323

Arrell, K., Wise, S., Wood, J., & Donoghue, D. (2008). Spectral filtering as a method of visualising and removing striped artefacts in digital elevation data. *Earth Surface Processes and Landforms*, *33*(6), 943–961. https://doi.org/10.1002/esp.1597

Asselman, N. E. M. (2000). Fitting and interpretation of sediment rating curves. *Journal of Hydrology*, *234*(3–4), 228–248. https://doi.org/10.1016/S0022-1694(00)00253-5

Becek, K. (2008). Investigating error structure of shuttle radar topography mission elevation data product. *Geophysical Research Letters*, *35*(15), L15403. https://doi.org/10.1029/2008GL034592

Ben-Israel, M., Armon, M., Aster Team, & Matmon, A. (2022). Sediment residence times in large rivers quantified using a cosmogenic nuclides-based transport model and implications for buffering of continental erosion signals. *Journal of Geophysical Research: Earth Surface*, *127*(5), e2021JF006417. https://doi.org/10.1029/2021JF006417

Besl, P. J., & McKay, N. D. (1992). A method for registration of 3-D shapes. *IEEE Transactions on Pattern Analysis and Machine Intelligence*, *14*(2), 239–256. https://doi.org/10.1109/34.121791

Booth, A. M., Roering, J. J., & Perron, J. T. (2009). Automated landslide mapping using spectral analysis and high-resolution topographic data: Puget Sound lowlands, Washington, and Portland Hills, Oregon. *Geomorphology*, *109*(3–4), 132–147. https://doi.org/10.1016/j.geomorph.2009.02.027

Brasington, J., Vericat, D., & Rychkov, I. (2012). Modeling river bed morphology, roughness, and surface sedimentology using high resolution terrestrial laser scanning. *Water Resources Research*, *48*(11), W11519. https://doi.org/10.1029/2012WR012223

Capart, H., Hsu, C., Lai, J., & Hsieh, M. L. (2010). Formation and decay of a tributary-dammed lake, Laonong River, Taiwan. *Water Resources Research*, *46*(11). https://doi.org/10.1029/2010WR009159

Carabajal, C. C., & Harding, D. J. (2005). ICESat validation of SRTM C-band digital elevation models. *Geophysical Research Letters*, *33*(22), L22S01. https://doi.org/10.1029/2005GL023957

Carretier, S., Regard, V., Leanni, L., Farías, M., Maffre, P., & Bonnet, S. (2020). The distribution of sediment residence times at the foot of mountains and its implications for proxies recorded in sedimentary basins. *Earth and Planetary Science Letters*, *546*, 116448. https://doi.org/10.1016/j.epsl.2020.116448

Chen, C., Hollingsworth, J., Clark, M. K., Chamlagain, D., Bista, S., Zekkos, D., et al. (2025). Erosional cascade during the 2021 Melamchi flood. *Nature Geoscience*, *18*(1), 32–36. https://doi.org/10.1038/s41561-024-01596-x

Chen, R., Lin, C., Chen, Y., He, T., & Fei, L. (2015). Detecting and characterizing active thrust fault and deep-seated landslides in dense Forest areas of Southern Taiwan using airborne LiDAR DEM. *Remote Sensing*, *7*(11), 15443–15466. https://doi.org/10.3390/rs71115443

Chen, Y., & Medioni, G. (1992). Object modelling by registration of multiple range images. *Image and Vision Computing*, *10*(3), 145–155. https://doi.org/10.1016/0262-8856(92)90066-C

Chen, Y.-C., Chang, K.-T., Lee, H.-Y., & Chiang, S.-H. (2014). Average landslide erosion rate at the watershed scale in southern Taiwan estimated from magnitude and frequency of rainfall. *Geomorphology*, *228*, 756–764. https://doi.org/10.1016/j.geomorph.2014.07.022

Clapp, E. M., Bierman, P. R., Schick, A. P., Lekach, J., Enzel, Y., & Caffee, M. (2000). Sediment yield exceeds sediment production in arid region drainage basins. *Geology*, *28*(11), 995–998. https://doi.org/10.1130/0091-7613(2000)28<995:SYESPI>2.0.CO;2

Clift, P. D., & Giosan, L. (2014). Sediment fluxes and buffering in the post-glacial Indus Basin. *Basin Research*, *26*(3), 369–386. https://doi.org/10.1111/bre.12038

Covault, J. A., Craddock, W. H., Romans, B. W., Fildani, A., & Gosai, M. G. (2013). Spatial and temporal variations in landscape evolution: Historic and longer-term sediment flux through global catchments. *The Journal of Geology*, *121*(1), 31–49. https://doi.org/10.1086/668680

Crippen, R., Buckley, S., Agram, P., Belz, E., Gurrola, E., Hensley, S., et al. (2016). NASADEM global elevation model: Methods and progress. *The International Archives of the Photogrammetry, Remote Sensing and Spatial Information Sciences*, *41*, 125–128. https://doi.org/10.5194/isprs-archives-XLI-B4-125-2016

CSRSR. (2024). SPOT satellite images [Dataset]. *Center for Space and Remote Sensing Research, National Central University*. Retrieved from https://opendata.csrsr.ncu.edu.tw/index.aspx

Dadson, S. J., Hovius, N., Chen, H., Dade, W. B., Hsieh, M.-L., Willett, S. D., et al. (2003). Links between erosion, runoff variability, and seismicity in the Taiwan orogen. *Nature*, *426*(6967), 648–651. https://doi.org/10.1038/nature02150

Dadson, S. J., Hovius, N., Chen, H., Dade, W. B., Lin, J.-C., Hsu, M.-L., et al. (2004). Earthquake-triggered increase in sediment delivery from an active mountain belt. *Geology*, *32*(8), 733–736. https://doi.org/10.1130/G20639.1

Daley, J. S., Brooks, A. P., & Spencer, J. R. (2024). Comment on "Assessing gully erosion and rehabilitation using multi temporal LiDAR DEMs: Case study from the Great Barrier Reef catchments, Australia" by Khan et al., 2023. *International Soil and Water Conservation Research*, *12*(2), 481–486. https://doi.org/10.1016/j.iswcr.2023.09.001

Dedkov, A. (2004). The relationship between sediment yield and drainage basin area. In *Sediment transfer through the fluvial System: Proceedings of the international symposium* (pp. 197–204). IAHS Press. Moscow, Russia, *2-6 August 2004* (IAHS Publication No. 288.

DeLisle, C., Yanites, B. J., Chen, C.-Y., Shyu, J. B. H., & Rittenour, T. M. (2022). Extreme event-driven sediment aggradation and erosional buffering along a tectonic gradient in southern Taiwan. *Geology*, *50*(1), 16–20. https://doi.org/10.1130/G49304.1

Derrieux, F., Siame, L. L., Bourlès, D. L., Chen, R. F., Braucher, R., Léanni, L., et al. (2014). How fast is the denudation of the Taiwan mountain belt? Perspectives from in situ cosmogenic ^{10}Be. *Journal of Asian Earth Sciences*, *88*, 230–245. https://doi.org/10.1016/j.jseaes.2014.03.012

Dickinson, W. T. (1981). *Accuracy and precision of suspended sediment loads* (Vol. 133, pp. 195–202). International Association of Hydrological Sciences Publication.

East, A. E., Logan, J. B., Dartnell, P., Lieber-Kotz, O., Cavagnaro, D. B., McCoy, S. W., & Lindsay, D. N. (2021). Watershed sediment yield following the 2018 carr fire, Whiskeytown National Recreation Area, Northern California. *Earth and Space Science*, *8*(9), e2021EA001828. https://doi.org/10.1029/2021EA001828

East, A. E., & Sankey, J. B. (2020). Geomorphic and sedimentary effects of modern climate change: Current and anticipated future conditions in the Western United States. *Reviews of Geophysics*, *58*(4), e2019RG000692. https://doi.org/10.1029/2019RG000692

Ehlers, T. A., & Farley, K. A. (2003). Apatite (U-Th)/He thermochronometry: Methods and applications to problems in tectonic and surface processes. *Earth and Planetary Science Letters*, *206*(1–2), 1–14. https://doi.org/10.1016/S0012-821X(02)01069-5

European Space Agency. (2024). Copernicus global digital elevation model [Dataset]. *OpenTopography*. https://doi.org/10.5069/G9028PQB

Ferguson, R. I. (1986). River loads underestimated by rating curves. *Water Resources Research*, *22*(1), 74–76. https://doi.org/10.1029/WR022i001p00074

Fryirs, K., Brierley, G. J., & Erskine, W. D. (2012). Use of ergodic reasoning to reconstruct the historical range of variability and evolutionary trajectory of rivers. *Earth Surface Processes and Landforms*, *37*(7), 763–773. https://doi.org/10.1002/esp.3210

Fuller, C. W., Willett, S. D., Fisher, D., & Lu, C. Y. (2006). A thermomechanical wedge model of Taiwan constrained by fission-track thermochronometry. *Tectonophysics*, *425*(1–4), 1–24. https://doi.org/10.1016/j.tecto.2006.05.018

Fuller, C. W., Willett, S. D., Hovius, N., & Slingerland, R. (2003). Erosion rates for Taiwan mountain basins: New determinations from suspended sediment records and a stochastic model of their temporal variation. *Journal of Geology*, *111*(1), 71–87. https://doi.org/10.1086/344665

Gellis, A. C., Hereford, R., Schumm, S. A., & Hayes, B. R. (2004). Channel evolution and hydrologic variations in the Colorado River basin: Factors influencing sediment and salt loads. *Journal of Hydrology*, *124*(3–4), 317–344. https://doi.org/10.1016/0022-1694(91)90215-G

German Aerospace Center (DLR). (2023). TanDEM-X 30m edited DEM (EDEM) [Dataset]. *EOC Geoservice*. Retrieved from https://download.geoservice.dlr.de/TDM30_EDEM/

Gesch, D., Oimoen, M., Danielson, J., & Meyer, D. (2016). Validation of the ASTER Global Digital Elevation Model Version 3 over the conterminous United States. *The International Archives of the Photogrammetry, Remote Sensing and Spatial Information Sciences*, *XLI-B4*, 143–148. https://doi.org/10.5194/isprs-archives-XLI-B4-143-2016

González, C., Bachmann, M., Bueso-Bello, J.-L., Rizzoli, P., & Zink, M. (2020). A fully automatic algorithm for editing the TanDEM-X global DEM. *Remote Sensing*, *12*(23), 3961. https://doi.org/10.3390/rs12233961

Google Earth Pro. (2024). Historical imagery [Software]. *Google LLC*. Retrieved from https://earth.google.com

Granger, D. E., Lifton, N. A., & Willenbring, J. K. (2013). A cosmic trip: 25 years of cosmogenic nuclides in geology. *Geological Society of America Bulletin*, *125*(9–10), 1379–1402. https://doi.org/10.1130/B30774.1

Grieve, S. W. D., Mudd, S. M., Milodowski, D. T., Clubb, F. J., & Furbish, D. J. (2016). How does grid-resolution modulate the topographic expression of geomorphic processes? *Earth Surface Dynamics*, *4*(3), 627–653. https://doi.org/10.5194/esurf-4-627-2016

GSMMA. (2023). Landslide cloud [Dataset]. *Geological Survey and Mining Management Center, MOEA*. Retrieved from http://landslide.geologycloud.tw/map/zh-tw

Guth, P. L., & Geoffroy, T. M. (2021). LiDAR point cloud and ICESat-2 evaluation of 1 second global digital elevation models: Copernicus wins. *Transactions in GIS*, *25*(5), 2245–2261. https://doi.org/10.1111/tgis.12825

Halsted, C. T., Bierman, P. R., Codilean, A. T., Corbett, L. B., & Caffee, M. W. (2025). Global analysis of in situ cosmogenic 26Al and 10Be and inferred erosion rate ratios in modern fluvial sediments indicates widespread sediment storage and burial during transport. *Geochronology*, *7*(3), 213–228. https://doi.org/10.5194/gchron-7-213-2025

Hansen, M. C., Potapov, P. V., Moore, R., Hancher, M., Turubanova, S. A., Tyukavina, A., et al. (2013). High-resolution global maps of 21st-century forest cover change. *Science*, *342*(6160), 850–853. https://doi.org/10.1126/science.1244693

Hassan, M. A., Church, M., Lisle, T. E., Brardinoni, F., Benda, L., & Grant, G. E. (2005). Sediment transport and channel morphology of small, forested streams. *JAWRA Journal of the American Water Resources Association*, *41*(4), 853–876. https://doi.org/10.1111/j.1752-1688.2005.tb03773.x

Hawker, L., Uhe, P., Paulo, L., Sosa, J., Savage, J., Sampson, C., et al. (2022). Fabdem V1-2 [Dataset]. *University of Bristol*. https://doi.org/10.5523/bris.s5hqmjcdj8yo2ibzi9b4ew3sn

Henny, L., Thorncroft, C. D., Hsu, H.-H., & Bosart, L. F. (2021). Extreme rainfall in Taiwan: Seasonal statistics and trends. *Journal of Climate*, *34*(12), 4711–4731. https://doi.org/10.1175/JCLI-D-20-0999.1

Hoffmann, T. (2015). Sediment residence time and connectivity in non-equilibrium and transient geomorphic systems. *Earth-Science Reviews*, *150*, 609–627. https://doi.org/10.1016/j.earscirev.2015.07.008

Hovius, N., Stark, C. P., & Allen, P. A. (1997). Sediment flux from a mountain belt derived by landslide mapping. *Geology*, *25*(3), 231–234. https://doi.org/10.1130/0091-7613(1997)025<0231:sffamb>2.3.co;2

Hsieh, M.-L., & Capart, H. (2013). Late Holocene episodic river aggradation along the Lao-nong River (southwestern Taiwan): An application to the Tseng-wen Reservoir Transbasin Diversion Project. *Engineering Geology*, *159*, 83–97. https://doi.org/10.1016/j.enggeo.2013.03.019

Hsieh, Y.-C., Chan, Y.-C., & Hu, J.-C. (2016). Digital elevation model differencing and error estimation from multiple sources: A case study from the Meiyuan Shan landslide in Taiwan. *Remote Sensing*, *8*(3), 199. https://doi.org/10.3390/rs8030199

Hugonnet, R., McNabb, R., Berthier, E., Menounos, B., Nuth, C., Girod, L., & Kaab, A. (2022). Uncertainty analysis of digital elevation models by spatial inference from stable terrain. *IEEE Journal of Selected Topics in Applied Earth Observations and Remote Sensing*, *15*, 6456–6472. https://doi.org/10.1109/JSTARS.2022.3188922

James, L. A. (1999). Time and the persistence of alluvium: River engineering, fluvial geomorphology, and mining sediment in California. *Geomorphology*, *31*(1–4), 265–290. https://doi.org/10.1016/S0169-555X(99)00084-7

James, L. A., Hodgson, M. E., Ghoshal, S., & Latiolais, M. M. (2012). Geomorphic change detection using historic maps and DEM differencing: The temporal dimension of geospatial analysis. *Geomorphology*, *137*(1), 181–198. https://doi.org/10.1016/j.geomorph.2010.10.039

Japan Aerospace Exploration Agency. (2021). ALOS World 3D 30 meter DEM V3.2 [Dataset]. *JAXA Earth Observation Research Center*. Retrieved from https://www.eorc.jaxa.jp/ALOS/en/dataset/aw3d30/aw3d30_e.htm

Kao, S.-J., Lee, T.-Y., & Milliman, J. D. (2005). Calculating highly fluctuated suspended sediment fluxes from mountainous rivers in Taiwan. *Terrestrial, Atmospheric and Oceanic Sciences*, *16*(3), 653–675. https://doi.org/10.3319/TAO.2005.16.3.653(T)

Kao, S.-J., & Milliman, J. D. (2008). Water and sediment discharge from small mountainous rivers, Taiwan: The roles of lithology, episodic events, and human activities. *Journal of Geology*, *116*(5), 431–448. https://doi.org/10.1086/590921

Kemp, D. B., Sadler, P. M., & Vanacker, V. (2020). The human impact on North American erosion, sediment transfer, and storage in a geologic context. *Nature Communications*, *11*(1), 6012. https://doi.org/10.1038/s41467-020-19744-3

Kenyi, L. W., Dubayah, R., Hofton, M., & Schardt, M. (2009). Comparative analysis of SRTM–NED vegetation canopy height to LIDAR-derived vegetation canopy metrics. *International Journal of Remote Sensing*, *30*(11), 2797–2811. https://doi.org/10.1080/01431160802555853

Kirchner, J. W., Finkel, R. C., Riebe, C. S., Granger, D. E., Clayton, J. L., King, J. G., & Megahan, W. F. (2001). Mountain erosion over 10 yr, 10 ky, and 10 my time scales. *Geology*, *29*(7), 591–594. https://doi.org/10.1130/0091-7613(2001)029<0591:meoyky>2.0.co;2

Kumar, G. (2026). 2020 edition Numerical Terrain model (DTM) data for the Laonong River Basin [Dataset]. *Zenodo*. https://doi.org/10.5281/zenodo.19625289

Kumar, G., Chan, Y.-C., Sun, C.-W., & Chen, C.-T. (2024). Decadal-scale assessment of sediment denudation rates in the Zhoukou River Basin, Taiwan: Insights from improved DEMs of differencing based on spectral analysis. *Geomatics, Natural Hazards and Risk*, *15*(1), 2363428. https://doi.org/10.1080/19475705.2024.2363428

Leenman, A., & Tunnicliffe, J. (2019). Tributary-junction fans as buffers in the sediment cascade: A multi-decadal study. *Earth Surface Processes and Landforms*, *45*(2), 265–279. https://doi.org/10.1002/esp.4717

Li, D., Lu, X., Overeem, I., Walling, D. E., Syvitski, J., Kettner, A. J., et al. (2021). Exceptional increases in fluvial sediment fluxes in a warmer and wetter High Mountain Asia. *Science*, *374*(6567), 599–603. https://doi.org/10.1126/science.abi9649

Li, F.-C., Angelier, J., Chen, R.-F., Hsieh, H.-M., Deffontaines, B., Luo, C.-R., et al. (2005). Estimates of present-day erosion based on sediment transport in rivers: A case study in Taiwan. *Comptes Rendus Geoscience*, *337*(13), 1131–1139. https://doi.org/10.1016/j.crte.2005.05.001

Li, K., Ma, R., Jiang, L., Liu, K., & Song, C. (2022). Accuracy assessment of high-resolution globally available open-source DEMs using ICESat/GLAS over mountainous areas: A case study in Yunnan Province, China. *Remote Sensing*, *15*(7), 1952. https://doi.org/10.3390/rs15071952

Li, Y., Huang, C., Wang, B., Tian, Z., & Chen, W. (2021). Increasing sediment discharge with rising temperatures in high mountain Asia. *Environmental Research Letters*, *16*(6), 064059. https://doi.org/10.1088/1748-9326/ac0b00

Li, Y. H. (1976). Denudation of Taiwan island since the Pliocene epoch. *Geology*, *4*(2), 105–107. https://doi.org/10.1130/0091-7613(1976)4<105:DOTIST>2.0.CO;2

Lin, C.-W., Chuang, Y.-C., Chang, W.-S., Liu, S.-H., & Shieh, C.-L. (2020). Geomorphological analysis of landslide distribution in Taiwan. *Geomorphology*, *354*, 107037. https://doi.org/10.1016/j.geomorph.2020.107037

Lin, L.-Y., Lin, C.-T., Chen, Y.-M., Cheng, C.-T., Li, H.-C., & Chen, W.-B. (2022). The Taiwan climate change projection information and adaptation knowledge platform: A decade of climate research. *Water*, *14*(3), 358. https://doi.org/10.3390/w14030358

Lindsay, J. B., Francioni, A., & Cockburn, J. M. (2019). LiDAR DEM smoothing and the preservation of drainage features. *Remote Sensing*, *11*(16), 1926. https://doi.org/10.3390/rs11161926

Lisle, T. E., Cui, Y., Parker, G., Pizzuto, J. E., & Dodd, A. M. (2001). The dominance of dispersion in the evolution of bed material waves in gravel-bed rivers. *Earth Surface Processes and Landforms*, *26*(13), 1409–1420. https://doi.org/10.1002/esp.300

Lo, P.-C., Lo, W., Chiu, Y.-C., & Wang, T.-T. (2021). Movement characteristics of a creeping slope influenced by river erosion and aggradation: Study of Xinwulü River in southeastern Taiwan. *Engineering Geology*, *295*, 106443. https://doi.org/10.1016/j.enggeo.2021.106443

Lp Daac (2019). ASTER Global Digital Elevation Model (GDEM) Version 3 [Dataset]. *NASA EOSDIS Land Processes DAAC*. https://asterweb.jpl.nasa.gov/gdem.asp

Marc, O., & Hovius, N. (2015). Amalgamation in landslide maps: Effects and automatic detection. *Natural Hazards and Earth System Sciences*, *15*(4), 723–733. https://doi.org/10.5194/nhess-15-723-2015

Marešová, J., Bašta, P., Gdulová, K., Barták, V., Kozhoridze, G., Šmída, J., et al. (2024). Choosing the optimal global digital elevation model for stream network delineation: Beyond vertical accuracy. *Earth and Space Science*, *11*(12), e2024EA003743. https://doi.org/10.1029/2024EA003743

Maune, D. F. (Ed.) (2007). *Digital elevation model technologies and applications: The DEM users manual* (2nd ed.). American Society for Photogrammetry and Remote Sensing.

Mesa-Mingorance, J. L., & Ariza-López, F. J. (2020). Accuracy assessment of digital elevation models (DEMs): A critical review of practices of the past three decades. *Remote Sensing*, *12*(16), 2630. https://doi.org/10.3390/rs12162630

Micheletti, N., & Lane, S. N. (2016). Water yield and sediment export in small, partially glaciated Alpine watersheds in a warming climate. *Water Resources Research*, *52*(6), 4924–4943. https://doi.org/10.1002/2016WR018774

Milliman, J. D., & Farnsworth, K. L. (2011). *River discharge to the coastal ocean: A global synthesis*. Cambridge University Press. https://doi.org/10.1017/CBO9780511781247

Molnar, P., & England, P. (1990). Late Cenozoic uplift of mountain ranges and global climate change: Chicken or egg? *Nature*, *346*(6279), 29–34. https://doi.org/10.1038/346029a0

NASA JPL. (2013). NASADEM shuttle radar topography mission global 1 arc second (version 003) [Dataset]. *NASA EOSDIS Land Processes Distributed Active Archive Center*. https://doi.org/10.5067/MEaSUREs/SRTM/SRTMGL1.003

NASA JPL. (2020). NASADEM merged DEM global 1 arc second (version 001) [Dataset]. *NASA EOSDIS Land Processes DAAC*. https://doi.org/10.5067/MEaSUREs/NASADEM/NASADEM_HGT.001

Nuth, C., & Kääb, A. (2011). Co-registration and bias corrections of satellite elevation data sets for quantifying glacier thickness change. *The Cryosphere*, *5*(1), 271–290. https://doi.org/10.5194/tc-5-271-2011

Okolie, C. J., Mills, J. P., Adeleke, A. K., Smit, J. L., Peppa, M. V., Altunel, A. O., & Arungwa, I. D. (2024). Assessment of the global Copernicus, NASADEM, ASTER and AW3D digital elevation models in Central and Southern Africa. *Geo-Spatial Information Science*, *27*(4), 1362–1390. https://doi.org/10.1080/10095020.2023.2296010

O'Loughlin, F. E., Paiva, R. C., Durand, M., Alsdorf, D. E., & Bates, P. D. (2016). A multi-sensor approach towards a global vegetation corrected SRTM DEM product. *Remote Sensing of Environment*, *182*, 49–59. https://doi.org/10.1016/j.rse.2016.04.018

Papalexiou, S. M., & Montanari, A. (2019). Global and regional increase of precipitation extremes under global warming. *Water Resources Research*, *55*(6), 4901–4914. https://doi.org/10.1029/2018WR024067

Perron, J. T., Kirchner, J. W., & Dietrich, W. E. (2008). Spectral signatures of characteristic spatial scales and nonfractal structure in landscapes. *Journal of Geophysical Research*, *113*(F4), F04003. https://doi.org/10.1029/2007JF000866

Pimenova, N., Norouzi, H., & Kussul, N. (2022). Regional "Bare-Earth" digital terrain model for Costa Rica based on NASADEM corrected for vegetation bias. *Remote Sensing*, *14*(10), 2421. https://doi.org/10.3390/rs14102421

Prieur, C., Godard, V., & Bourlès, D. L., & ASTER Team. (2025). Climate-driven acceleration of denudation in the European Alps. *Earth and Planetary Science Letters*, *581*, 117405. https://doi.org/10.1016/j.epsl.2022.117405

Purinton, B. (2026). bpurinton/DEM_fourier_noise: V1.0.0 — Initial Zenodo release (v1.0.0) [Software]. *Zenodo*. https://doi.org/10.5281/zenodo.19807252

Purinton, B., & Bookhagen, B. (2017). Validation of digital elevation models (DEMs) and comparison of geomorphic metrics on the southern Central Andean Plateau. *Earth Surface Dynamics*, *5*(2), 211–237. https://doi.org/10.5194/esurf-5-211-2017

Purinton, B., & Bookhagen, B. (2018). Measuring decadal vertical land-level changes from SRTM-C (2000) and TanDEM-X (~2015) in the south-central Andes. *Earth Surface Dynamics*, *6*(4), 971–987. https://doi.org/10.5194/esurf-6-971-2018

Purinton, B., & Bookhagen, B. (2021). Beyond vertical point accuracy: Assessing inter-pixel consistency in 30 m global DEMs for the arid Central Andes. *Frontiers in Earth Science*, *9*, 758606. https://doi.org/10.3389/feart.2021.758606

Reiners, P. W., & Brandon, M. T. (2006). Using thermochronology to understand orogenic erosion. *Annual Review of Earth and Planetary Sciences*, *34*(1), 419–466. https://doi.org/10.1146/annurev.earth.34.031405.125202

Roering, J. J., Kirchner, J. W., & Dietrich, W. E. (1999). Evidence for nonlinear, diffusive sediment transport on hillslopes and implications for landscape morphology. *Water Resources Research*, *35*(3), 853–870. https://doi.org/10.1029/1998WR900090

Rolstad, C., Haug, T., & Denby, B. (2009). Spatially integrated geodetic glacier mass balance and its uncertainty based on geostatistical analysis: Application to the western Svartisen ice cap, Norway. *Journal of Glaciology*, *55*(192), 666–680. https://doi.org/10.3189/002214309789470950

Rosenholm, D., & Torlegård, K. (1988). Three-dimensional absolute orientation of stereo models using digital elevation data. *Photogrammetric Engineering and Remote Sensing*, *54*(10), 1385–1389.

Ruetenik, G. A., Ferrier, K. L., & Marc, O. (2024). Decadal-scale decay of landslide-derived fluvial suspended sediment after Typhoon Morakot. *Earth Surface Dynamics*, *12*(4), 863–881. https://doi.org/10.5194/esurf-12-863-2024

Sadler, P. M., & Jerolmack, D. J. (2015). Scaling laws for aggradation, denudation and progradation rates: The case for time-scale invariance at sediment sources and sinks. *Geological Society*, *404*(1), 69–88. https://doi.org/10.1144/SP404.7

Schwat, E., Istanbulluoglu, E., Horner-Devine, A., Anderson, S., Knuth, F., & Shean, D. (2023). Multi-decadal erosion rates from glacierized watersheds on Mount Baker, Washington, USA, reveal topographic, climatic, and lithologic controls on sediment yields. *Geomorphology*, *438*, 108805. https://doi.org/10.1016/j.geomorph.2023.108805

Shean, D. E., Alexandrov, O., Moratto, Z. M., Smith, B. E., Joughin, I. R., Porter, C., & Morin, P. (2016). An automated, open-source pipeline for mass production of digital elevation models (DEMs) from very-high-resolution commercial stereo satellite imagery. *ISPRS Journal of Photogrammetry and Remote Sensing*, *116*, 101–117. https://doi.org/10.1016/j.isprsjprs.2016.03.008

Singer, M. B., Aalto, R., James, L. A., Kilham, N. E., Higson, J. L., & Ghoshal, S. (2013). Enduring legacy of a toxic fan via episodic redistribution of California gold mining debris. *Proceedings of the National Academy of Sciences*, *110*(46), 18436–18441. https://doi.org/10.1073/pnas.1302295110

Sklar, L. S., & Dietrich, W. E. (2004). A mechanistic model for river incision into bedrock by saltating bed load. *Water Resources Research*, *40*(6), W06301. https://doi.org/10.1029/2003WR002496

Stark, C. P., & Guzzetti, F. (2009). Landslide rupture and the probability distribution of mobilized debris volumes. *Journal of Geophysical Research*, *114*(F2), F00A02. https://doi.org/10.1029/2008JF001008

Su, Y., Guo, Q., Xue, B., Hu, T., Alvarez, O., Tao, S., & Fang, J. (2015). SRTM DEM correction in vegetated mountain areas through the integration of spaceborne LiDAR, airborne LiDAR, and optical imagery. *Remote Sensing*, *7*(9), 11202–11228. https://doi.org/10.3390/rs70911202

Tachikawa, T., Kaku, M., Iwasaki, A., Gesch, D. B., Oimoen, M. J., Zhang, Z., et al. (2011). ASTER Global Digital Elevation Model version 2—Summary of validation results. *Sioux Falls, SD: NASA*.

Tadono, T., Ishida, H., Oda, F., Naito, S., Minakawa, K., & Iwamoto, H. (2014). Precise global DEM generation by ALOS PRISM. *ISPRS Annals of the Photogrammetry, Remote Sensing and Spatial Information Sciences*, *II-4*, 71–76. https://doi.org/10.5194/isprsannals-II-4-71-2014

Tseng, C.-M., Chang, K.-J., & Chen, Y.-S. (2019). Evaluation of landslide yielding sediments by using multi-temporal high resolution topographies. In *Proceedings of the XVII european conference on soil mechanics and geotechnical engineering (ECSMGE-2019)* (pp. 1–8). European Conference on Soil Mechanics and Geotechnical Engineering.

Tseng, C.-W., Song, C.-E., Wang, S.-F., Chen, Y.-C., Tu, J.-Y., Yang, C.-J., & Chuang, C.-W. (2020). Application of high-resolution radar rain data to the predictive analysis of landslide susceptibility under climate change in the Laonong watershed, Taiwan. *Remote Sensing*, *12*(23), 3855. https://doi.org/10.3390/rs12233855

Tsou, C.-Y., Feng, Z.-Y., Chigira, M., & Matsushi, Y. (2011). Catastrophic landslides induced by Typhoon Morakot in southern Taiwan: Their types and mechanisms. *Landslides*, *8*(2), 191–207. https://doi.org/10.1007/s10346-011-0251-8

Tunnicliffe, J., Brierley, G., Fuller, I. C., Leenman, A., Marden, M., & Peacock, D. (2018). Reaction and relaxation in a coarse-grained fluvial system following catchment-wide disturbance. *Geomorphology*, *307*, 50–64. https://doi.org/10.1016/j.geomorph.2017.10.007

Tyukavina, A., Hansen, M. C., Potapov, P. V., Stehman, S. V., Smith-Rodriguez, K., Okpa, C., et al. (2015). Aboveground carbon loss in natural and managed tropical forests from 2000 to 2012. *Environmental Research Letters*, *10*(7), 074002. https://doi.org/10.1088/1748-9326/10/7/074002

Uhe, P., Hawker, L., Paulo, L., Sosa, J., Sampson, C., & Neal, J. (2022). FABDEM - A 30m global map of elevation with forests and buildings removed. *EGU General Assembly 2022*. 23-27 May 2022, EGU22-8994. https://doi.org/10.5194/egusphere-egu22-8994

Üstün, A., Abbak, R. A., & Zeray Öztürk, E. (2016). Height biases of SRTM DEM related to EGM96: From a global perspective to regional practice. *Survey Review*, *50*(358), 26–35. https://doi.org/10.1080/00396265.2016.1218159

Van Zyl, J. J. (2001). The Shuttle Radar Topography Mission (SRTM): A breakthrough in remote sensing of topography. *Acta Astronautica*, *48*(5–12), 559–565. https://doi.org/10.1016/S0094-5765(01)00020-0

von Blanckenburg, F. (2006). The control mechanisms of erosion and weathering at basin scale from cosmogenic nuclides in river sediment. *Earth and Planetary Science Letters*, *242*(3–4), 224–239. https://doi.org/10.1016/j.epsl.2005.11.017

Walling, D. E. (1983). The sediment delivery problem. *Journal of Hydrology*, *65*(1–3), 209–237. https://doi.org/10.1016/0022-1694(83)90217-2

Walling, D. E., & Fang, D. (2003). Recent trends in the suspended sediment loads of the world's rivers. *Global and Planetary Change*, *39*(1–2), 111–126. https://doi.org/10.1016/S0921-8181(03)00020-9

Weng, M., Wu, M., Ning, S., & Jou, Y. (2011). Evaluating triggering and causative factors of landslides in Lawnon River Basin, Taiwan. *Engineering Geology*, *123*(1–2), 72–82. https://doi.org/10.1016/j.enggeo.2011.07.001

Wessel, B. (2018). *TanDEM-X ground segment - DEM products specification document (issue 3.2)*. EOC, DLR. Retrieved from https://tandemx-science.dlr.de/

Wheaton, J. M., Brasington, J., Darby, S. E., & Sear, D. A. (2010). Accounting for uncertainty in DEMs from repeat topographic surveys: Improved sediment budgets. *Earth Surface Processes and Landforms*, *35*(2), 136–156. https://doi.org/10.1002/esp.1886

Willett, S. D. (1999). Orogeny and orography: The effects of erosion on the structure of mountain belts. *Journal of Geophysical Research*, *104*(B12), 28957–28981. https://doi.org/10.1029/1999JB900248

Williams, R. D. (2012). DEMs of difference. In *Geomorphological techniques: Vol. section 3.2* (pp. 1–17). British Society for Geomorphology.

Wittmann, H., von Blanckenburg, F., Maurice, L., Guyot, J.-L., Filizola, N., & Kubik, P. W. (2011). Sediment production and delivery in the Amazon River basin quantified by in situ-produced cosmogenic nuclides and recent river loads. *GSA Bulletin*, *123*(5–6), 934–950. https://doi.org/10.1130/B30317.1